

# Humidity lightens the air—but hinders human evaporative cooling in arid heat

Shri H. Viswanathan<sup>1</sup>, Ankit Joshi,<sup>1,2</sup> Isabella DeClair,<sup>1</sup> Bryce Twidwell,<sup>1</sup> Muhammad Abdullah,<sup>3</sup> Lyle Bartels,<sup>1,4</sup> Faisal Abedin,<sup>1</sup> Joseph Rotella,<sup>1</sup> Cibin T. Jose,<sup>1</sup> and Konrad Rykaczewski<sup>1,2</sup>

1. School for Engineering of Matter, Transport and Energy, Arizona State University, Tempe, AZ 85287, USA
2. Julie Ann Wrigley Global Futures Laboratory, Arizona State University, Tempe, AZ 85287, USA
3. School of Sustainability, Arizona State University, Tempe, AZ, USA
4. Thermetrics, LLC, Seattle, WA, USA

**Corresponding author:** Konrad Rykaczewski

**Email:**[konradr@asu.edu](mailto:konradr@asu.edu)

## Author Contributions:

K.R. and S.H.V. designed research; S.H.V., A.J., I.D.C., B.T., M.A., L.B., C.T.J., F.A., J.R. performed research; S.H.V. and K.R., analyzed data and wrote the paper; all authors performed review and editing of the paper

**Keywords:** Free Convection, Sweat Evaporation, Buoyancy Effects, Multiphysics Modeling, Human Thermoregulation Modeling

## Abstract

Overheating poses significant threats to human health and productivity. In hot conditions, the human body primarily cools through sweat evaporation; however, we show that understanding of physical phenomena controlling the evaporation rate is surprisingly incomplete. This rate is equal to the product of the skin-to-air water vapor concentration difference and the flow-dependent mass transfer coefficient, which, according to the Lewis heat-and-mass transfer analogy, is proportional to the convective heat transfer coefficient. In low-wind, free-convection conditions, current models for the human heat transfer coefficients consider only temperature-driven air buoyancy. Here, we show that in arid heat, humidity from sweat exerts a comparable but opposing buoyant effect. Using sweating thermal manikin experiments and digital-twin multiphysics simulations, we demonstrate that the dueling thermal and humidity-induced buoyancy can severely suppress sweat evaporation (e.g., by over half in conditions that occur in Arizona for one-third of the year). Neglecting humidity-induced buoyancy leads to substantial errors in thermoregulation model predictions—within 2-hour exposure to typical arid heat conditions, core temperature increases by 1 °C more than predicted by legacy calculations. We provide compact, physics-informed models for free-convective heat transfer coefficients for wide temperature and humidity ranges, enabling improved thermoregulation modeling and thermal audits for more accurate heat-stress assessment and optimization of extreme heat mitigation strategies.

Overheating poses an escalating threat to human health and productivity. Sweat evaporation is the body's principal cooling pathway, yet we will show that quantitative understanding of this vital and ubiquitous process remains incomplete. This knowledge gap follows a historical trend: comprehension of sweat evaporation and its key role in thermoregulation often lagged other scientific advancements. For instance, in 1912, while Einstein was formulating the general theory of relativity, the Portuguese marathoner Francisco Lázaro (1) believed that sweating hindered performance and coated his body with wax and fat, fatally succumbing to heatstroke during the Olympic race. A decade later, Lewis (2) introduced the classical theory linking convective heat and mass transfer (**SI Appendix, Text S1**), but it took two decades for it to be applied to estimate human sweat evaporation rates (3, 4). Assuming sweat to be an isothermal film at the temperature of the underlying skin, which is valid for low evaporation rates after about 15 minutes from the onset of sweating (5, 6)—the Lewis analogy states that the evaporative heat flux ( $Q_e$ ,  $W \cdot m^{-2}$ ) can be expressed as (7, 8):

$$Q_e = h_e(p_{sk} - p_{air})\omega = 16.5h_c(p_{sk} - p_{air})\omega \quad \text{Eq.1}$$

Where  $\omega$  is the fraction of wet skin,  $h_c$  ( $W \cdot m^{-2} \cdot K^{-1}$ ) is the convective heat transfer coefficient, and  $h_e$  ( $W \cdot m^{-2} \cdot kPa^{-1}$ ) is the corresponding evaporative mass transfer coefficient with units adjusted for the driving humidity difference expressed in terms of partial pressure of water vapor (kPa) of skin ( $p_{sk} = C_{sk}R(T_{sk} + 273.15)/M_w$  where  $C_{sk}$  is the vapor concentration ( $kg \cdot m^{-3}$ ),  $R = 8.314 J \cdot mol^{-1} \cdot K^{-1}$  is the universal gas constant, and  $M_w = 18.02 g \cdot mol^{-1}$  is the molecular weight of water) and ambient air ( $p_{air}$ ). For forced convection, this direct relationship between  $h_c$  and  $h_e$  can be readily confirmed using a thermal manikin in a climate-controlled chamber with a wind tunnel or its digital twin (see **Fig. 1A-B, SI Appendix, Text S2, Fig. S1A–F, and Fig. S2**). In contrast, we will show that, under free convection in arid heat conditions, the standard “textbook” models for the heat transfer coefficient employed for over seven decades diverge sharply from experimental observations.

At negligible wind speeds, the difference in air density at the skin surface and in the environment creates a buoyant force that drives a near-skin airflow and free convective heat and mass transfer. Since the 1950s (8–10), free-convective heat transfer, and therefore  $Q_e$ , from the human body has been modeled solely as a consequence of thermal buoyancy, driven by skin-to-air temperature differences ( $\Delta T_{sk-air} = T_{sk} - T_{air}$ ). When ambient air temperature exceeds dry skin temperature, the cooled air adjacent to the skin becomes denser and descends, generating downward convection. However, in hot and dry conditions, humidity from evaporating sweat exerts an equally important but opposing influence on air density near wet skin (**Fig. 1C**). Specifically, humid air is lighter than dry air—saturated air at 35 °C near wet skin is roughly 15% lighter than dry air at the same temperature but 10% relative humidity (RH)—producing upward buoyant flow. For wet skin surrounded by hotter and drier air, these thermal (downward) and humidity (upward) driven buoyancies oppose one another, at times canceling to yield neutral buoyancy and flow stagnation (e.g., 41 °C air at 10% RH). Such “dueling buoyancy” phenomena are well recognized in engineering contexts (11–14), but they remain entirely overlooked in human physiological modeling and heat stress assessment (7).

Although forced convection dominates in outdoor heat-stress scenarios (15, 16), free convection governs most indoor environments—where people spend ~87% of their time (17, 18). Indoor temperatures often exceed ASHRAE comfort limits (20–27.5 °C) (19, 20), impairing cognition (21, 22), reducing productivity, and worsening heat-related illness. For example, in 2024, Maricopa County, Arizona, reported 138 indoor heat-related deaths (out of 608 total), 88% of which occurred in homes without functional cooling (23). Similar conditions arise in semi-outdoor spaces such as tents (24), warehouses, and construction sites—settings where sweat evaporation is critical to preventing overheating but evidently is poorly characterized.

Here, we quantify the dueling buoyancy effects on free convection and sweat evaporation from the human body using comprehensive sweating thermal manikin experiments and digital-twin multiphysics simulations. In experiments, multiple heat transfer mechanisms—namely, free convection, evaporation, and radiation—contribute simultaneously to the net heat flux measured by the sweating thermal manikin.

Consequently, matching digital twin simulations are required to isolate and quantify the contribution of each mechanism. We highlight that while this manikin represents an anthropometrically average male, we previously found that body shape has a minor impact on the convective heat transfer coefficient (25, 26). We further show that standard "temperature difference-only" models overpredict free convective heat transfer and sweat evaporation rates, leading to a substantial underestimation of physiological heat stress in arid heat. To enable more accurate heat-stress assessments and improved design of mitigation strategies for extreme-heat environments, we develop compact, physics-informed models for human free-convective heat transfer valid across wide temperature and humidity ranges.

## Results

### ***Multiphysics digital twin agrees with thermal manikin measurements in diverse conditions***

To validate our digital manikin twin, we performed a comprehensive series of thermal manikin experiments under conditions designed to generate buoyant near-body flow through temperature-only, humidity-only, and combined temperature–humidity effects. A multiphysics digital twin replicating the experimental setup was developed using COMSOL Multiphysics software by coupling “Turbulent Fluid Flow”, “Heat Transfer in Fluids”, “Surface-to-Surface Radiation” and “Moisture Transport” physics modules. Experiments were conducted inside a nearly sealed enclosure that limited ambient air motion to below  $0.02 \text{ m}\cdot\text{s}^{-1}$  (**Fig. 1A**) located within a climate-controlled chamber where air temperature ( $T_{air}$ ) and relative humidity ( $RH_{air}$ ) were systematically varied (see **Methods** and **SI Appendix, Text S3** for details). The manikin’s surface temperature ( $T_{sk}$ ) was set to  $35 \text{ }^\circ\text{C}$ , representative of typical human skin (8). To isolate thermally driven free convection, the manikin surface was kept dry (no sweating) while  $T_{air}$  was varied ( $40.3\text{--}44.8 \text{ }^\circ\text{C}$ ) at constant absolute humidity. Unlike earlier studies focused on cold-to-moderate environments ( $T_{air}$ :  $20.1\text{--}29.1 \text{ }^\circ\text{C}$ ) (7, 25, 27)—where the body generates an upward buoyant plume—our conditions featured  $T_{air} > T_{sk}$  (moderate-to-hot), resulting in downward free convection (**Fig. 1B**). To isolate only humidity-driven evaporation, the temperatures of the air and water-saturated manikin textile “skin” were set to  $35 \text{ }^\circ\text{C}$ , while only  $RH_{air}$  was varied (**Fig. 1A, Inset**). Finally, combined temperature and humidity effects were explored by increasing  $T_{air}$  by  $4.6 \text{ }^\circ\text{C}$  or  $7.5 \text{ }^\circ\text{C}$  above the water-saturated manikin surface temperature while varying humidity. The results in **Fig. 1D** show that the whole-body net heat flux predicted by the digital twin ( $Q_{Sim-WB}$ ,  $\text{W}\cdot\text{m}^{-2}$ ) closely matches the measured values ( $Q_{Exp-WB}$ ,  $\text{W}\cdot\text{m}^{-2}$ ) across all tested conditions. Comparable agreement was observed for 35 individual body segments, with the any moderate segment-level deviations and their causes detailed in **SI Appendix, Text S3** (see **Fig. S3A–F**, **Fig. S4A–B**, **Fig. S5A–D**, **Fig. S6A–D**, and **Fig. S7A–D**). Having validated the model, we next employ the digital twin to quantify the coupled influence of temperature and humidity on free convection coefficients and sweat evaporation rates over a broad range of environmental conditions.

### ***How temperature and humidity impact sweat evaporation rates and free convection coefficients***

With the experimentally validated digital twin, we systematically explored the influence of dueling buoyancies on free convection and sweat evaporation for an average western male by parametrically varying  $T_{air}$  ( $20\text{--}50 \text{ }^\circ\text{C}$ ) and  $RH_{air}$  ( $10\text{--}90\%$ ) (100 cases total, simulated using High Performance Research Computing facilities at Arizona State University (28)), while maintaining a water-saturated skin surface at  $35 \text{ }^\circ\text{C}$  (**Fig. S8A–C**). **Fig. 2A** compares the simulated whole-body free convective coefficients ( $h_{sim}$ ,  $\text{W}\cdot\text{m}^{-2}\cdot\text{K}^{-1}$ ) against the "temperature-difference only" free convective empirical formulations,  $h_{\Delta T\text{-only}} = 1.36 |\Delta T_{sk-air}|^{0.3}$  ( $\text{W}\cdot\text{m}^{-2}\cdot\text{K}^{-1}$ ), derived from our prior cold-to-moderate studies (25) and validation cases (moderate-to-hot). Additionally, the individual buoyant forces arising from the temperature ( $\Delta T_{sk-air} = T_{sk} - T_{air}$ ) and humidity concentration ( $\Delta C_{sk-air} = C_{sk} - C_{air}$ ) differences, namely,  $B_{\Delta T} = g\rho\beta_T\Delta T_{sk-air}$  and  $B_{\Delta C} = g\rho\beta_C\Delta C_{sk-air}$ , were also computed (see **SI Appendix, Text S4**, **Fig. S9A–C**, **Fig. S10A–C**, and **Fig. S11A–C**). Here  $g$  is the gravitational acceleration ( $9.81 \text{ m}\cdot\text{s}^{-2}$ ),  $\beta_T$  is the thermal coefficient of expansion (reciprocal of the absolute average of  $T_{air}$  and  $T_{sk}$ ), and  $\beta_C$  is the coefficient of expansion due to compositional changes.

$\beta_C$  can be obtained from the density of air ( $\rho$ ), the average molecular weight of air ( $MW_a = 29 \text{ g}\cdot\text{mol}^{-1}$ ), and that of water vapor ( $MW_C = 18.02 \text{ g}\cdot\text{mol}^{-1}$ ) as  $(MW_a/MW_C - 1)/\rho$  or  $0.607/\rho$  (11). We note that this study was restricted to cases with a positive skin-to-air moisture difference ( $C_{sk} > C_{air}$ ); scenarios with  $C_{sk} < C_{air}$ , which would cause condensation on the skin, were omitted.

Depending on ambient conditions, the coupled thermal- and humidity-driven buoyancies can either enhance or suppress free convection and sweat evaporation. When air is cooler than skin, both buoyancies are positive (**Table S4**) and act mutually to drive a stronger ascending plume ( $\rho_{sk} < \rho_{air}$ ), leading to enhanced heat and mass transfer, i.e., the coupled temperature- and humidity-differences driven  $h_{sim}$  exceeds the temperature difference-only driven  $h_{\Delta T-only}$  by up to 70.7% (34 °C air at 10% RH). In contrast, when  $T_{air}$  exceeds  $T_{sk}$ , the buoyancies oppose each other. For small temperature differences, the humidity-driven  $B_{\Delta C}$  dominates, driving an upward plume and leading to  $h_{sim} > h_{\Delta T-only}$ . As  $T_{air}$  substantially becomes hotter than the skin, the opposition between  $B_{\Delta T}$  and  $B_{\Delta C}$  intensifies, thereby progressively weakening the plume and hindering the heat transfer. Eventually, the two buoyancies nearly balance out each other ( $B_{\Delta T} \approx B_{\Delta C}$ ), thus creating a near-stagnant flow regime. Here, the simultaneous occurrence of moisture transport leads to maximum suppression of the heat transfer, making  $h_{sim}$  reach its lowest value. For instance, when air is at 41 °C and 10% RH,  $h_{sim}$  ( $1.01 \text{ W}\cdot\text{m}^{-2}\cdot\text{K}^{-1}$ ) is 56.4% lower than  $h_{\Delta T-only}$  ( $2.29 \text{ W}\cdot\text{m}^{-2}\cdot\text{K}^{-1}$ ). Across all cases, near-stagnation conditions produced  $h_{sim}$  values between  $0.71 \text{ W}\cdot\text{m}^{-2}\cdot\text{K}^{-1}$  (35.5 °C air at 90% RH) and  $1.26 \text{ W}\cdot\text{m}^{-2}\cdot\text{K}^{-1}$  (39 °C air at 30% RH). As the  $RH_{air}$  increases, the temperature at which the buoyancies balance each other shifts closer to the skin temperature, consistent with the fact that air at 35 °C and 100% RH (assuming mean  $T_{sk}$  across body surface is also 35 °C), nullifies both temperature and humidity differences, yielding an “ultimate” near-stagnation condition, with no free convection or sweat evaporation. With  $T_{air}$  rising beyond the stagnation condition,  $B_{\Delta T}$  overtakes  $B_{\Delta C}$ , thus reversing the flow to a descending plume. Yet, as  $B_{\Delta C}$  continues to oppose,  $h_{sim}$  remains suppressed relative to  $h_{\Delta T-only}$ . Overall, these findings highlight the critical transition from supportive to opposing interactions between the temperature- and humidity-driven buoyancies and their suppressive effect on the free convection in hot, arid conditions—effects overlooked by standard empirical formulations.

The coupled buoyancies influenced sweat evaporation in parallel. **Fig. 2B** compares the simulated evaporative heat fluxes ( $Q_{sim}$ ,  $\text{W}\cdot\text{m}^{-2}$ ) with the standard “textbook” estimate of evaporative heat flux ( $Q_{\Delta T-only}$ ,  $\text{W}\cdot\text{m}^{-2}$ ), which is conventionally computed as the product of  $h_{\Delta T-only}$ , Lewis factor ( $16.5 \text{ K}\cdot\text{kPa}^{-1}$ , (8)) and the skin-to-air vapor pressure differences, as prescribed by the Chilton-Colburn analogy (29) and Lewis relation (2, 30). Across all  $RH_{air}$ , when the air temperature is cooler than 25 °C,  $Q_{sim}$  is, slightly lower than  $Q_{\Delta T-only}$  (2.4–14.3%), by an average of  $18 \text{ W}\cdot\text{m}^{-2}$ . Between 30–35 °C, since the buoyancies reinforce each other, sweat evaporation is enhanced. For instance, air at 34 °C and 10% RH,  $Q_{sim}$  ( $188.7 \text{ W}\cdot\text{m}^{-2}$ ), is 65.2% higher than  $Q_{\Delta T-only}$  ( $114.2 \text{ W}\cdot\text{m}^{-2}$ ). However, as  $T_{air}$  becomes hotter, the competing temperature and humidity differences increasingly hinder the sweat evaporation, eventually bringing the plume to a near-stagnant condition and significantly suppressing the evaporation rates by almost 56% at 41 °C and 10% RH relative to the standard values ( $Q_{sim} = 82.4 \text{ W}\cdot\text{m}^{-2}$ ,  $Q_{\Delta T-only} = 182.7 \text{ W}\cdot\text{m}^{-2}$ ). Beyond the stagnation conditions, at higher humidities (lower vapor pressure differences), both  $Q_{sim}$  and  $Q_{\Delta T-only}$  are smaller, and the differences between them are smaller as well (see **SI Appendix, Text S4, Fig. S12A–F, Fig. S13A–F, and Fig. S14A–F** for individual  $RH_{air}$  plots).

## Discussion

### **Physics-informed free convection model accounting for humidity-induced buoyancy**

For water vapor diffusion in air at 35 °C, the Prandtl number (ratio of momentum to heat diffusivities,  $\nu/\alpha = 0.68$ ) and the Schmidt number (ratio of momentum to mass diffusivities,  $\nu/D = 0.66$ ) are approximately equal. Therefore, the Nusselt number ( $Nu = h_c L/k$ , where  $L$  (m) is the characteristic dimension and  $k$  ( $\text{W}\cdot\text{m}^{-1}\cdot\text{K}^{-1}$ ) is the thermal conductivity of air), representing the non-dimensional free

convective coefficient during simultaneous heat and water vapor transfer, can be calculated from the classical correlations using the total Rayleigh ( $Ra_T$ ) number, which is the sum of its thermal ( $Ra_{\Delta T}$ ) and concentration ( $Ra_{\Delta C}$ ) components (31):

$$Ra_T = Ra_{\Delta T} + Ra_{\Delta C} = \frac{g\beta_T\Delta T_{sk-air}L^3}{\nu\alpha} + \frac{g\beta_C\Delta C_{sk-air}L^3}{\nu D} \quad \text{Eq.2}$$

For free convection from a vertical plate, the Nusselt number follows (32):

$$Nu = 0.59Ra_T^{\frac{1}{4}} (10^4 < Ra_T < 10^9, \text{ laminar}) \quad \text{Eq.3}$$

$$Nu = 0.1Ra_T^{\frac{1}{3}} (10^9 < Ra_T < 10^{13}, \text{ turbulent}) \quad \text{Eq.4}$$

Our previous work showed that the whole-body free convective coefficients under thermally driven conditions are about 10% higher than predicted for turbulent free convection over a vertical plate of height 1.8 m (i.e., the manikin height) (25). Based on this, we recast all simulation outcomes in terms of the Nusselt number and corresponding  $Ra_T$ . **Fig. 3A** demonstrates that the non-dimensionalized simulation results align well with the classical vertical-plate correlations, especially for laminar flow. Our earlier studies based on thermally driven free convection covered  $Ra_{\Delta T}$  of  $2 \times 10^9$  to  $7 \times 10^9$ , where the data overlaps both the laminar and turbulent correlations (25). Expanding this range to  $|Ra_T|$  of  $4 \times 10^6$  to  $1.1 \times 10^{10}$  reveals that the laminar correlation with 1/4 exponent provides a substantially more universal fit. **Fig. 3A** also demonstrates an interesting feature of the simultaneous heat and mass transfer from the human body in a free convective regime: even as  $Ra_T \rightarrow 0$ , the  $Nu$  retains an albeit small, but finite value. This phenomenon occurs when  $\Delta T_{sk-air}$  and  $\Delta C_{sk-air}$  are non-zero but generate opposing buoyancy forces that cancel each other, creating a stagnant medium ( $Ra_T \rightarrow 0$ ), so heat and mass transfer occur through diffusion only (corresponding to a baseline  $Nu_0$ ). Therefore, we propose the following functional form for the Nusselt number for free convection from a sweaty human body:

$$Nu = Nu_0 + C|Ra_T|^{1/4} \quad \text{Eq.5}$$

Fitting our simulation data to **Eq. 5** matching the laminar coefficient, yields  $C = 0.568 \pm 0.012$  (68% CI) and  $Nu_0 = 18.56 \pm 2.88$  (68% CI). Supporting our physical reasoning for the stagnant flow case, a simulated "diffusion only" (i.e., no flow) value of  $Nu_0 = \frac{1.8h_0}{k} = 19.2$  closely agrees. To facilitate the application and interpretation of **Eq. 5**, we express it in terms of the heat transfer coefficient:

$$h_c = \frac{k}{L}Nu = \frac{k}{L}Nu_0 + \frac{kL^{3/4}}{L}C \left| \frac{g\beta_T\Delta T_{sk-air}}{\nu\alpha} + \frac{g\beta_C\Delta C_{sk-air}}{\nu D} \right|^{1/4} \quad \text{Eq.6}$$

Simplifying with air properties at 35 °C gives:

$$h_c = 0.275 + 1.25|\Delta T_{sk-air} + 164\Delta C_{sk-air}|^{1/4} \quad \text{Eq.7}$$

As shown in **Fig. 3B**, the model from **Eq. 7** predicts the 100 simulated cases very well ( $R^2 = 0.998$ ).

A generalized form of the equation can be written as:

$$h_c = h_0 + B|\Delta T_{sk-air} + 164\Delta C_{sk-air}|^{1/4} \quad \text{Eq.8}$$

Here,  $h_0$  is the diffusion-only value,  $B$  is the coefficient specifying geometrical, flow, and fluid property impacts, and  $\Delta T_{sk-air} + 164\Delta C_{sk-air}$  is the combined temperature and concentration buoyancy driving term. Fitting this physics-informed model to individual body segments also yields excellent agreement with the simulation results (see **Table 1**, **SI Appendix**, **Text S5**, **Fig. S15A–F**, **Fig. S16A–F**, and **Fig. S17A–F**).

In contrast to the whole-body coefficients, we observed substantial differences for regional values depending on flow direction. This observation reflects the fact that the boundary layer grows in the flow direction, leading to the highest heat transfer near the start of the flow or at the point where the flow transitions to turbulence. To maintain continuity in  $h_c$  when  $Ra_T$  changes sign, we first fitted **Eq. 8** to the positive  $Ra_T$  values. We used the resulting  $h_0$  values as inputs into corresponding fits for the negative  $Ra_T$  values (leaving  $B$  as the only fitting parameter). In either case, **Table 1** and plots described in the **SI Appendix**, **Text S5** (**Fig. S15A–F**, **Fig. S16A–F**, and **Fig. S17A–F**) show that the fitted models provide excellent match with the simulated segmental  $h_c$ .

## **Neglecting humidity-induced buoyancy leads to substantial errors in thermoregulation model predictions and dangerously overoptimistic heat stress assessments**

To assess the effects of humidity-driven buoyancy on thermophysiological responses, we employed our recently updated version of the classical six-segment Stolwijk thermoregulation model (10, 33). Simulations were performed under conditions representative of a semi-outdoor environment typical of Phoenix summers, using three approaches to calculate sweat evaporation under free convection conditions. Specifically, we simulated the thermophysiological responses of a lightly dressed (0.25 clo) average young male engaged in minimal exertion (1.5 Met) during a two-hour midday exposure inside a canopy-covered tent, with air at 41 °C and 20% RH, mean radiant temperature of 55 °C, and air velocity ( $U_{air}$ ,  $m \cdot s^{-1}$ ) under  $0.2 m \cdot s^{-1}$  (24). The three ways to compute sweat evaporation are, (A) constant  $h_c$  approach used in both versions of the Stolwijk model (10, 33), (B) temperature-difference driven approach ( $h_{\Delta T} = h = A(\Delta T_{sk-air})^{1/4}$ ), and (C) combined temperature- and humidity-difference driven approach ( $h_{\Delta T, \Delta C} = h = h_0 + B|\Delta T_{sk-air} + 164 \Delta C_{sk-air}|^{1/4}$ ) (see **Methods** for details). Predictions of the core temperature ( $T_{core}$ ) and mean skin temperature ( $\bar{T}_{sk}$ ) using the first two approaches differed by less than 0.15 °C; thus, we focus on comparing the temperature-difference ( $h_{\Delta T}$ ) and combined temperature- and humidity-difference driven ( $h_{\Delta T, \Delta C}$ ) approaches.

**Fig. 4A–B** show that neglecting humidity-driven buoyancy contributions results in a significant underprediction of thermophysiological responses. The  $h_{\Delta T}$  approach predicts that after 40 minutes, the  $T_{core}$  and  $\bar{T}_{sk}$  stabilize at about 37.9 °C and 37.0 °C, respectively. In contrast, the  $h_{\Delta T, \Delta C}$  approach predicts that the  $T_{core}$  and  $\bar{T}_{sk}$  continue to rise reaching 38.3 °C and 37.9 °C after 60 minutes, and 38.9 °C and 38.5 °C after 120 minutes. In other words, within 2 hours of arid heat exposure simulation, neglecting humidity-driven buoyancy effects leads to a dangerous underprediction of  $T_{core}$  by 1 °C and  $\bar{T}_{sk}$  by 1.5 °C.

The underlying physical mechanisms are clarified in **Fig. 4C–D**, which depict convective, radiative, evaporative, and metabolic heat rates, as well as net body heat storage. The mean buoyancy-driving terms ( $\overline{\Delta T}_{sk-air}$  vs.  $\overline{\Delta T}_{sk-air} + 164\overline{\Delta C}_{sk-air}$ ) for both approaches are also shown after scaling them by a factor of 50 for better visualization. In both cases, convective heat rates remain between 5 and 20 W, while radiative and metabolic rates remain near 160 W. During the first 10–20 minutes, sweat evaporation rapidly increases from approximately -15 W to -190 W for both models. In the  $h_{\Delta T}$  approach, the sweat evaporation rate continues to gradually increase to -280 W, with buoyancy driven by nearly constant  $\overline{\Delta T}_{sk-air}$  of -4 °C. As a result, the body heat storage rate drops below 50 W after 40 minutes and is almost eliminated after 60 minutes of heat exposure, leading to stabilization of the body temperatures. In contrast, in the  $h_{\Delta T, \Delta C}$  approach, the evaporation rate stalls due to nearly vanishing buoyancy with  $\overline{\Delta T}_{sk-air} + 164\overline{\Delta C}_{sk-air}$  between -1 °C to 0.5 °C. As a result, the body heat storage rate remains around 100 W for the first 60 minutes and does not drop below 50 W until 100 minutes of heat exposure, leading to increasing body temperatures. We note that the minor peaks in the evaporation rate in this case are due to switching of the  $\overline{\Delta T}_{sk-air} + 164\overline{\Delta C}_{sk-air}$  sign, and therefore a shift in the flow direction and the employed models from **Table 1**.

### **Limitations**

While this work provides a quantitative understanding of the coupled buoyancy effects, the findings rely on several assumptions that should be reiterated. First, the skin was modeled as uniformly water-saturated at 35 °C. In contrast, spatial variations in sweat rates and skin temperature (34) could generate heterogeneous vapor concentrations that, if accounted for, could further refine predicted convective coefficients. Second, our physics-informed model was derived for a static standing posture; alternative postures, such as seated or supine, can alter local driving differences and the resulting plume around the body. Local or whole-body movements (e.g., lifting packages in a warehouse) can locally induce mixed convection, highlighting the need to quantify postural and motion effects on convective coefficients in the future. Third, our model considers only direct skin-to-ambient heat exchange (a shamelessly naked manikin). Clothing can substantially affect the heat and mass transfer, particularly through complex

processes occurring within the skin-to-fabric microclimate (35–38). Therefore, in the future the complex buoyancy effects in presence of clothing should be investigated. Finally, the findings are based on an average western male body shape; therefore, exploring the impact of body shapes (including children, elderly, pregnant women, etc.) on the free convective coefficients, accounting for both thermal- and humidity-driven buoyancy effects, would further improve our understanding of human heat transfer.

### **Implications**

Our findings demonstrate that under hot (>37–38 °C) arid conditions with negligible airflow, the competing temperature- and humidity-driven buoyancies can suppress sweat evaporation by up to 56% (for air 41 °C with 10% RH). This phenomenon leads to substantially increased body heat storage and significantly elevated mean skin and core temperatures. Using classical temperature-difference based free convective heat transfer coefficient correlations result in thermoregulation models severely underpredicting this effect. Therefore, dueling buoyancy effects should be considered while estimating the risks of heat-related illness for vulnerable populations—including people who lack access to air-conditioning, residents of makeshift housing, and workers in poorly ventilated hot warehouses or construction sites. The proposed physics-informed models can be readily integrated into thermoregulation models (33, 39–43), thermal audit systems, and other heat stress assessment tools (7, 44). Accurate characterization of human thermophysiological responses in hot environments using these models can guide the design of improved heat-resilient spaces, heat-mitigation strategies, and targeted whole-body and local cooling solutions, thereby potentially helping to avert the rise in indoor heat-related deaths. The suppression of sweat evaporation during free convection in hot, arid conditions also provides additional motivation to use fans, potentially in a cyclical on-off mode in very hot conditions when continual forced convective heat gains exceed the benefits of evaporation (45, 46). Conversely, in moderate-to-cool conditions, the two buoyancies support each other, enhancing sweat evaporation and body cooling. Overall, the new insights on physical processes controlling sweat evaporation rate have broad implications for thermophysiological simulations helping to guide decisions impacting human health, safety, and productivity in hot arid climates.

### **Methods**

#### ***Thermal manikin experimentation***

To build a validated multiphysics model, a series of experiments (15 cases) were conducted inside a nearly sealed enclosure located within a climatic chamber (25) (**Fig. 1A** and **Fig. S3A–F**), using a 35-segmented sweating thermal manikin (ANDI from Thermetrics, LLC) representative of an average young western male (50<sup>th</sup> percentile height (m) and BMI (kg·m<sup>-2</sup>)). Three complementary sets of experiments—examining the individual effects of temperature-differences, humidity-differences, and combined temperature- and humidity-differences on free convection and sweat evaporation—were conducted by systematically varying the enclosure’s air temperature ( $T_{air}$ : 35–44.8 °C) and relative humidity ( $RH_{air}$ : 23.5–81.4%) (see **Table S3** for details). The manikin skin temperature was held uniformly at 35 °C with exception of 31 or 34 °C for temperature-difference only cases. For experiments involving sweat evaporation, a water-saturated (at 35 °C) textile “skin” (**Fig.1A** Inset) was used to maintain a wet skin fraction of 1. All 15 cases were repeated thrice, each lasting 75 minutes, and steady-state data collected from the final 30 minutes (segmental skin temperature fluctuations remained < 0.05 °C) were used to determine the whole-body ( $Q_{Exp-WB}$ , W·m<sup>-2</sup>) and zonal ( $Q_{Exp-Z}$ , W·m<sup>-2</sup>) heat fluxes (see **SI Appendix, Text S3** for details).

#### ***Multiphysics simulation for validation***

A digital twin of the experimental setup was developed in COMSOL Multiphysics 6.3. Since the entire setup was symmetrical, only one-half of the geometry was simulated, to reduce computational cost. The model comprised the “Turbulent Fluid Flow”, “Heat Transfer in Fluids”, “Surface-to-Surface Radiation” and “Moisture Transport” physics modules coupled through “Non-Isothermal flow”, “Heat and Moisture Transfer”, “Heat transfer with Surface-to-Surface radiation”, and “Moisture flow” multiphysics interfaces. A

Low-Re k- $\epsilon$  Turbulence model (with Low-Re wall functions) was used to capture near-skin flow features. Moist air was treated as weakly compressible flow and the gravity module was enabled to resolve the buoyancy-driven flow. Experimental boundary conditions were virtually replicated within the digital twin. To avoid numerical convergence issues (25), the inlet and outlet boundaries of the enclosure were dynamically assigned along the direction of the buoyant flow. For an ascending buoyant plume, the enclosure floor was set as the inlet and the ceiling as the outlet (vice versa for a descending plume, see **SI Appendix, Text S3** and **Fig. S4A**). Following the mesh refinement study (**Fig. S4B**), the model was solved transiently for 300 s. A quasi-steady state was achieved between 240 and 300 s, with net heat flux variations under 5%. The simulated net whole-body ( $Q_{Sim-WB}$ ,  $W \cdot m^{-2}$ ) and zonal ( $Q_{Sim-Z}$ ,  $W \cdot m^{-2}$ ) heat fluxes were compared to experimental measurements for validation (see **Fig. 1D**, **SI Appendix, Text S3**, **Fig. S5A–D**, **Fig. S6A–D**, and **Fig. S7A–D**).

### ***Parametric study using the validated multiphysics model***

The validated numerical model was used to investigate the coupled buoyancy effects by parametrically varying inlet  $T_{air}$  (20–50 °C) and  $RH_{air}$  (10–90%). Unlike the sealed enclosure, parametric study was performed within a simplified virtual enclosure (4 m length, 2 m width, 3 m height) with a watertight 3D geometry of an average young western male (50<sup>th</sup> percentile height and BMI) positioned at the geometric center (**Fig. S8A–B**). Radiative heat exchange was not analyzed for this study. After a mesh refinement analysis (**Fig. S8C**), the optimized mesh was initialized using a wall-distance method and solved transiently for 50 s, to compute the whole-body and regional free convective coefficients and evaporative fluxes. A quasi-steady state was achieved after 30s, with variations in free convective coefficients under 5% (see **SI Appendix, Text S4** for details).

### ***Thermoregulation modeling***

To analyze the impact of coupled thermal- and humidity-induced buoyancies on thermophysiological responses, we used the updated Stolwijk-2024 thermoregulation model, previously described and validated for multiple human heat exposure trials by Joshi et al. (33). In the present work, we focused on free convection conditions ( $U_{air} < 0.2 \text{ m} \cdot \text{s}^{-1}$ ) and quantified the effect of three approaches for modeling regional free convective coefficients ( $h_c$ ,  $W \cdot m^{-2} \cdot K^{-1}$ ). First approach used constant  $h_c$  values employed in the original Stolwijk model (10) and the newer ones introduced in JOS-2 and JOS-3 models (47) (**Table 2**). Second, a temperature-difference based approach was employed, where  $h_c$  was defined as  $A(\Delta T_{sk-air})^{1/4}$ . We used regional  $A$  values proposed by Wissler (7), representing averages of measurements reported by Quintela et al. (48) and de Dear et al. (27) (**Table 2**).  $h_c$  for hands and feet were unavailable in  $A(\Delta T_{sk-air})^{1/4}$  form. Hence, we fitted this form to the average of values predicted by the two correlations (right and left halves) reported by Quintela et al. (48, 49). This yielded  $A = 2.7$  for hands and  $A = 1.57$  for legs (see **SI Appendix, Text S6** and **Fig. S18A–B**).

Thirdly, a combined temperature- and humidity-difference based approach developed from the current study was used, where  $h_c$  was defined as  $h_0 + B|\Delta T_{sk-air} + 164 \Delta C_{sk-air}|^{1/4}$  (**Eq. 8**) with regional fitted parameters outlined in **Table 2**. We note that, hands were excluded from the validation simulations for the following reasons. Our physical manikin does not have heated fingers, therefore free convective coefficients for hands were not measured. Moreover, simulating convection around hands requires a dense mesh, specifically around the fingers (26) and the convective coefficients for the hands are highly dependent on pose and orientation. Hence, hands were not simulated in the convection models. Instead of our own measurements or simulations, for the hands we fitted **Eq. 8** to the average of the two correlations given by Quintela et al. (48), obtaining  $h_0 = 0.5$  and  $B = 2.4$  (**Fig. S18A** shows reasonable agreement between our fitted correlation and the average results of Quintela et al. (48)).



**Acknowledgments:**

This research was supported by the National Science Foundation #2152468 # 2214152 awards, while the thermal manikin was funded by a National Science Foundation Major Research Instrumentation grant #2117917. The authors gratefully acknowledge Research Computing at Arizona State University for providing high-performance computing resources that have contributed to the research results reported within this paper.

**Data Availability Statement:**

All data supporting the findings of this study are included in the main manuscript and the supporting information.

## References

1. Olympics, Francisco Lazaro. Available at <https://www.olympics.com/en/athletes/francisco-lazaro> (accessed 19 November 2025)
2. W. K. Lewis, The Evaporation of a Liquid Into a Gas. *Transactions of the American Society of Mechanical Engineers* 44, 325–332 (1922).
3. J. R. Murlin, Skin temperature, its measurement and significance for energy metabolism. *Ergeb Physiol* 42, 153–227 (1939).
4. S. R. Notley, D. Mitchell, N. A. S. Taylor, A century of exercise physiology: concepts that ignited the study of human thermoregulation. Part 1: Foundational principles and theories of regulation. *Eur J Appl Physiol* 123, 2379–2459 (2023).
5. C. T. Jose, *et al.*, A micro-to-macroscale and multi-method investigation of human sweating dynamics. *J R Soc Interface* 22 (2025).
6. A. K. Jaiswal, *et al.*, Simultaneous imaging of multi-pore sweat dynamics and evaporation rate measurement using wind tunnel ventilated capsule with infrared window. *iScience* 27, 110304 (2024).
7. E. H. Wissler, *Human Temperature Control* (Springer Berlin Heidelberg, 2018).
8. Ken Parsons, *Human thermal environments: the effects of hot, moderate, and cold environments on human health, comfort and performance* (CRC Press, 2014), pp. 167–169.
9. D. F. Brebner, D. McK. Kerslake, J. L. Waddell, The relation between the coefficients for heat exchange by convection and by evaporation in man. *J Physiol* 141, 164–168 (1958).
10. J. A. Stolwijk, “A Mathematical Model of Physiological Temperature Regulation in Man, NASA CR-1855” (1971).
11. B. Gebhart, L. Pera, The nature of vertical natural convection flows resulting from the combined buoyancy effects of thermal and mass diffusion. *Int J Heat Mass Transf* 14, 2025–2050 (1971).
12. M. Hasan, A. S. Mujumdar, Simultaneous heat and mass transfer in free convection from a horizontal cylinder. *AIAA Journal* 23, 1602–1608 (1985).
13. E. M. Sparrow, G. K. Kratz, M. J. Schuerger, Evaporation of Water From a Horizontal Surface by Natural Convection. *J Heat Transfer* 105, 469–475 (1983).
14. J. Schenk, R. Altmann, J. P. A. Wit, Interaction between heat and mass transfer in simultaneous natural convection about an isothermal vertical flat plate. *Applied Scientific Research* 32, 599–606 (1976).
15. K. Rykaczewski, *et al.*, A simple three-cylinder radiometer and low-speed anemometer to characterize human extreme heat exposure. *Int J Biometeorol* 68, 1081–1092 (2024).
16. A. Joshi, *et al.*, Characterization of human extreme heat exposure using an outdoor thermal manikin. *Science of the Total Environment* 923 (2024).
17. N. E. KLEPEIS, *et al.*, The National Human Activity Pattern Survey (NHAPS): a resource for assessing exposure to environmental pollutants. *J Expo Sci Environ Epidemiol* 11, 231–252 (2001).
18. Environmental Protection Agency (EPA), “Report to Congress on Indoor Air Quality: Volume 2, EPA/400/1-89/001C” (1989).
19. D. Khovalyg, *et al.*, Critical review of standards for indoor thermal environment and air quality. *Energy Build* 213, 109819 (2020).
20. ASHRAE, *ASHRAE Standard 55-2013: Thermal Environmental Conditions for Human Occupancy* (2013), pp. 12.

21. C. C. Hampo, L. H. Schinasi, S. Hoque, Surviving indoor heat stress in United States: A comprehensive review exploring the impact of overheating on the thermal comfort, health, and social economic factors of occupants. *Heliyon* 10, e25801 (2024).
22. J. G. Cedeño Laurent, *et al.*, Reduced cognitive function during a heat wave among residents of non-air-conditioned buildings: An observational study of young adults in the summer of 2016. *PLoS Med* 15, e1002605 (2018).
23. Maricopa County Department of Public Health, “2024 Heat-Related Deaths Report” (2025), (accessed 19 November 2025)
24. J. Karanja, *et al.*, Impact of tent shade on heat exposures and simulated heat strain for people experiencing homelessness. *Int J Biometeorol* 69, 2841–2854 (2025).
25. S. H. Viswanathan, *et al.*, Impact of human body shape on free convection heat transfer. *PLoS One* 20, e0318842 (2025).
26. S. H. Viswanathan, D. M. Martinez, L. Bartels, S. S. Guddanti, K. Rykaczewski, Impact of human body shape on forced convection heat transfer. *Int J Biometeorol* 67, 865–873 (2023).
27. R. de Dear, E. Arens, Z. Hui, M. Oguro, Convective and radiative heat transfer coefficients for individual human body segments. *International Journal of Biometeorology* 141–156 (1997).
28. D. M. Jennewein, *et al.*, The Sol Supercomputer at Arizona State University in *Practice and Experience in Advanced Research Computing*, (ACM, 2023), pp. 296–301.
29. T. H. Chilton, A. P. Colburn, Mass Transfer (Absorption) Coefficients Prediction from Data on Heat Transfer and Fluid Friction. *Ind Eng Chem* 26, 1183–1187 (1934).
30. Y. A. 'Ghajar, A. J. 'Çengel, *Heat and Mass Transfer: Fundamentals and Applications, 5th ed.* New York, NY. (McGraw-Hill, 2014), pp. 874–880.
31. S. W. Churchill, H. H. S. Chu, Correlating equations for laminar and turbulent free convection from a vertical plate. *Int J Heat Mass Transf* 18, 1323–1329 (1975).
32. T. L. Bergman, A. S. Lavine, F. P. Incropera, D. P. DeWitt, *Fundamentals of Heat and Mass Transfer, 7th ed.* New York, NY (John Wiley & Sons, Inc., , 2011), pp. 551–552.
33. A. Joshi, B. Twidwell, M. Park, K. Rykaczewski, Comparative analysis of thermoregulation models to assess heat strain in moderate to extreme heat. *J Therm Biol* 127, 104035 (2025).
34. C. J. Smith, G. Havenith, Body mapping of sweating patterns in male athletes in mild exercise-induced hyperthermia. *Eur J Appl Physiol* 111, 1391–1404 (2011).
35. K. Rykaczewski, Rational design of sun and wind shaded evaporative cooling vests for enhanced personal cooling in hot and dry climates. *Appl Therm Eng* 171 (2020).
36. A. Joshi, A. Psikuta, S. Annaheim, R. M. Rossi, Modelling of heat and mass transfer in clothing considering evaporation, condensation, and wet conduction with case study. *Build Environ* 228, 109786 (2023).
37. A. Joshi, A. Psikuta, M.-A. Bueno, S. Annaheim, R. M. Rossi, Effect of movement on convection and ventilation in a skin-clothing-environment system. *International Journal of Thermal Sciences* 166, 106965 (2021).
38. A. Joshi, A. Psikuta, M.-A. Bueno, S. Annaheim, R. M. Rossi, Analytical clothing model for sensible heat transfer considering spatial heterogeneity. *International Journal of Thermal Sciences* 145, 105949 (2019).
39. X. Xu, T. P. Rioux, M. P. Castellani, Three dimensional models of human thermoregulation: A review. *J Therm Biol* 112, 103491 (2023).

40. X. Xu, T. P. Rioux, J. W. Castellani, S. J. Montain, N. Charkoudian, Validation of livability environmental limits to heat and humidity. *J Appl Physiol* 137, 1642–1648 (2024).
41. X. Xu, *et al.*, Modeling thermoregulatory responses during high-intensity exercise in warm environments. *J Appl Physiol* 136, 908–916 (2024).
42. K. Katić, R. Li, W. Zeiler, Thermophysiological models and their applications: A review. *Build Environ* 106, 286–300 (2016).
43. D. Filingeri, N. Koch Esteves, How hot is too hot for people? A review of empirical models of perceptual, physiological and functional limits of human heat tolerance. *Exp Physiol* (2025). <https://doi.org/10.1113/EP092242>.
44. J. Vanos, *et al.*, A physiological approach for assessing human survivability and liveability to heat in a changing climate. *Nat Commun* 14, 7653 (2023).
45. D. Gagnon, S. A. Romero, M. N. Cramer, O. Jay, C. G. Crandall, Cardiac and Thermal Strain of Elderly Adults Exposed to Extreme Heat and Humidity With and Without Electric Fan Use. *JAMA* 316, 989 (2016).
46. N. M. Ravanelli, S. G. Hodder, G. Havenith, O. Jay, Heart Rate and Body Temperature Responses to Extreme Heat and Humidity With and Without Electric Fans. *JAMA* 313, 724 (2015).
47. Y. Takahashi, *et al.*, Thermoregulation model JOS-3 with new open source code. *Energy Build* 231, 110575 (2021).
48. D. Quintela, A. Gaspar, C. Borges, Analysis of sensible heat exchanges from a thermal manikin. *Eur J Appl Physiol* 92, 663–668 (2004).
49. M. Zhang, *et al.*, A 3D multi-segment thermoregulation model of the hand with realistic anatomy: Development, validation, and parametric analysis. *Build Environ* 201, 107964 (2021).

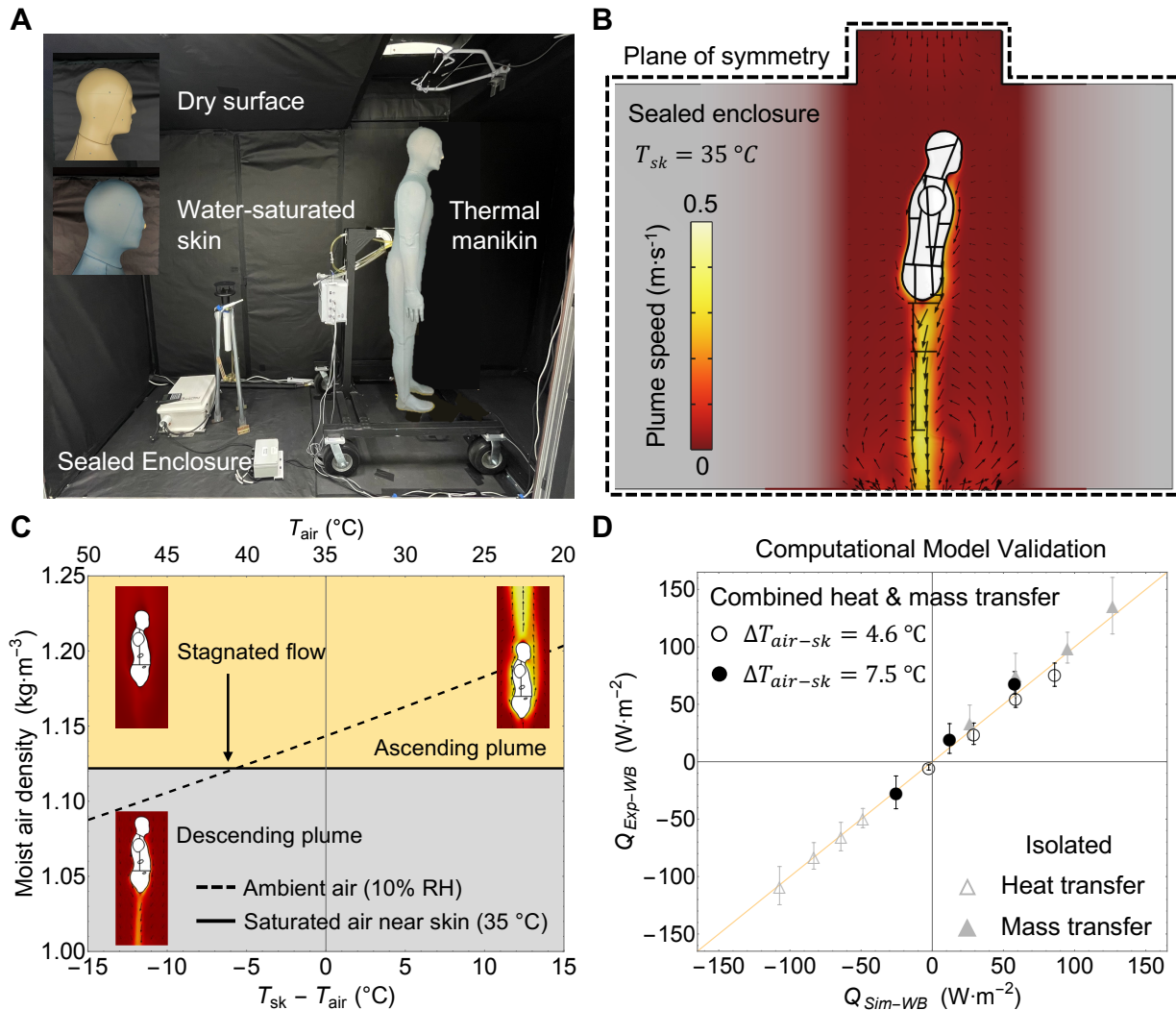


**Fig. 1. Experimental validation of the multiphysics numerical model.** (A) Experimental setup for investigating coupled-buoyancy effects on heat exchange with a sweating thermal manikin inside a nearly sealed enclosure located within a climatic chamber. Inset: Manikin surface fitted with a water-saturated textile “skin” during sweat evaporation experiments and left dry otherwise. (B) Cross-sectional side view of the manikin’s digital twin developed using a multiphysics numerical model. Inset: Partially illustrated descending buoyant plume simulated around the manikin when ambient air ( $T_{air}$ , °C) is hotter than the skin ( $T_{sk}$ , °C) with plume speeds ranging from 0 to 0.5 m·s<sup>-1</sup>. (C) Comparison of moist air density near and away from the water-saturated skin ( $T_{sk}$  at 35 °C), under varying  $T_{air}$  at 10% RH. Inset: Coupled thermal- and humidity-difference induced density variations leading to ascending, stagnant, and descending buoyant plume. (D) Simulated whole-body net heat fluxes ( $Q_{Sim-WB}$ , W·m<sup>-2</sup>) closely match experimental measurements ( $Q_{Exp-WB}$ , W·m<sup>-2</sup>) across all 15 cases—including isolated heat transfer, isolated mass transfer, and combined heat and mass transfer.  $\Delta T_{air-sk}$  (°C) is the air-to-skin temperature difference. Data points are averages of three replicates with 95% confidence intervals (combined Type A and B uncertainty).

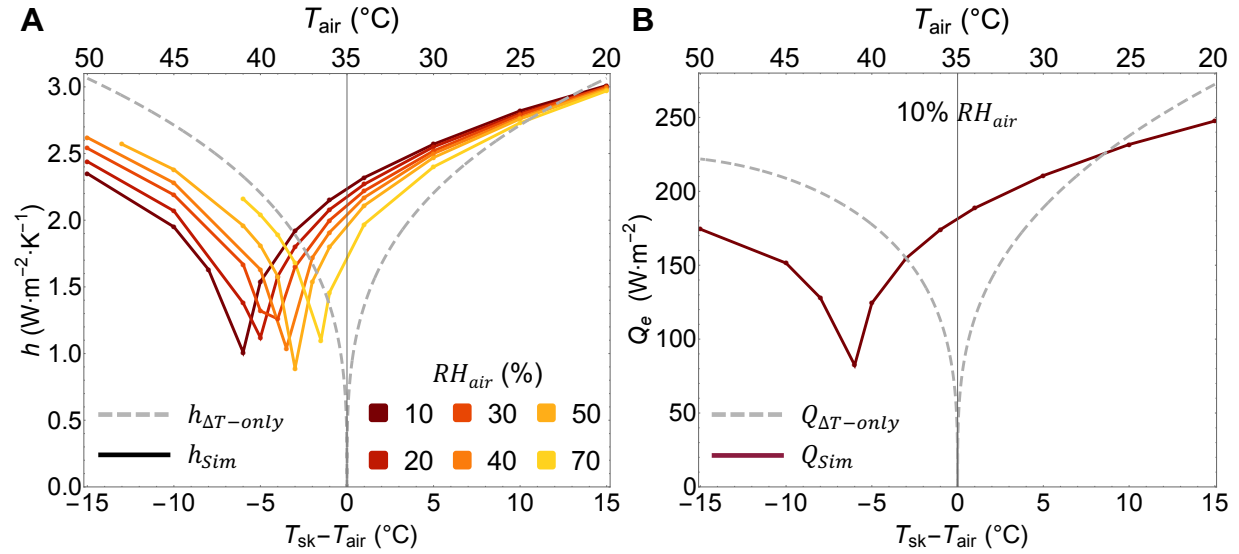


**Fig. 2. Coupled buoyancy effects on free convective heat transfer coefficient ( $h$ ,  $\text{W}\cdot\text{m}^{-2}\cdot\text{K}^{-1}$ ) and sweat evaporation flux ( $Q_e$ ,  $\text{W}\cdot\text{m}^{-2}$ ).** Simulated whole-body (A) free convective coefficients heat transfer coefficients ( $h_{sim}$ ,  $\text{W}\cdot\text{m}^{-2}\cdot\text{K}^{-1}$ ) and (B) evaporative fluxes ( $Q_{sim}$ ,  $\text{W}\cdot\text{m}^{-2}$ ) are compared with temperature-difference based empirical correlations across a range of air temperatures ( $T_{air}$ ,  $^{\circ}\text{C}$ ) and selected relative humidities ( $RH_{air}$ ). The empirical correlations are  $h_{\Delta T-only} = 1.36 |\Delta T_{sk-air}|^{0.3}$  ( $\text{W}\cdot\text{m}^{-2}\cdot\text{K}^{-1}$ ) for free convection (25), and  $Q_{\Delta T-only} = 16.5 h_{\Delta T-only} \Delta p_{sk-air}$  ( $\text{W}\cdot\text{m}^{-2}$ ) for evaporative heat flux (8), where  $\Delta T_{sk-air}$  ( $^{\circ}\text{C}$ ) and  $\Delta p_{sk-air}$  (kPa) are the skin-to-air temperature and vapor pressure differences, respectively.

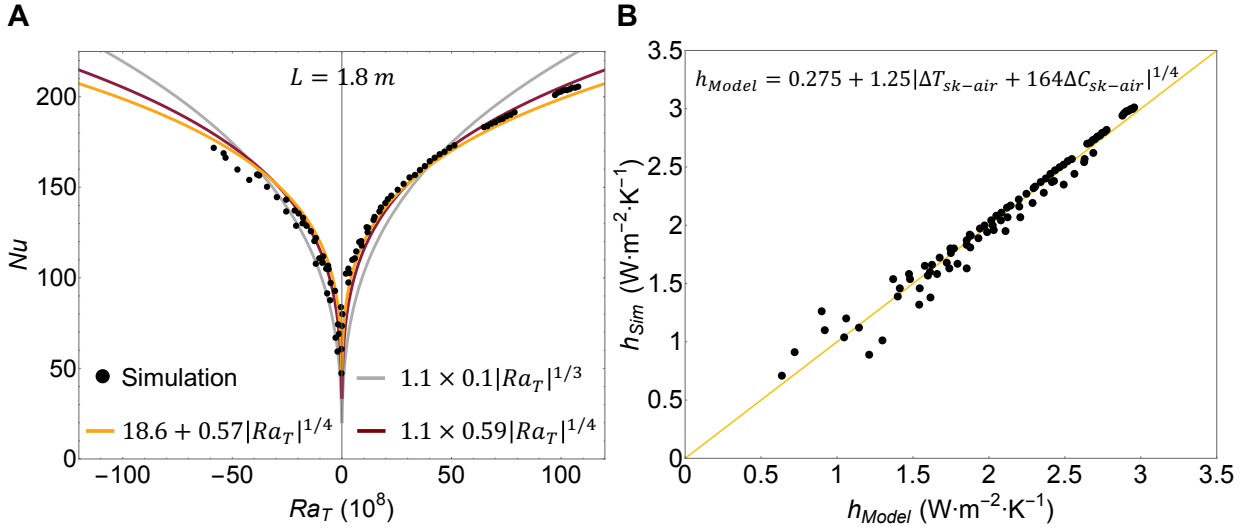


**Fig. 3. Comparison of the non-dimensional and dimensional free convection coefficients against classical correlations and model predictions. (A)** The non-dimensional simulated whole-body free convection coefficients ( $h_{Sim}$ ,  $W \cdot m^{-2} \cdot K^{-1}$ ), expressed as a Nusselt number ( $Nu$ ), follows the fitted relation  $Nu = 18.6 + 0.57 |Ra_T|^{1/4}$  (Eq. 5), where  $Ra_T$  is the total Rayleigh number. The fitted trend closely aligns with the classical laminar vertical-plate correlations  $Nu = 1.1 \times 0.59 |Ra_T|^{1/4}$  (Eq. 3, (32)) than with turbulent flow correlations  $Nu = 1.1 \times 0.1 |Ra_T|^{1/3}$  (Eq. 4, (32)). Characteristic length ( $L$ ) of 1.8 m was used (manikin height) while fitting. **(B)** Simulated whole-body free convective coefficients ( $h_{Sim}$ ,  $W \cdot m^{-2} \cdot K^{-1}$ ) strongly agree with the physics-informed model predictions ( $h_{Model}$ ,  $W \cdot m^{-2} \cdot K^{-1}$ , Eq. 8), across all 100 simulated ambient conditions.  $\Delta T_{sk-air}$  ( $^{\circ}C$ ) and  $\Delta C_{sk-air}$  ( $kg \cdot m^{-3}$ ) are the skin-to-air temperature and concentration differences respectively.

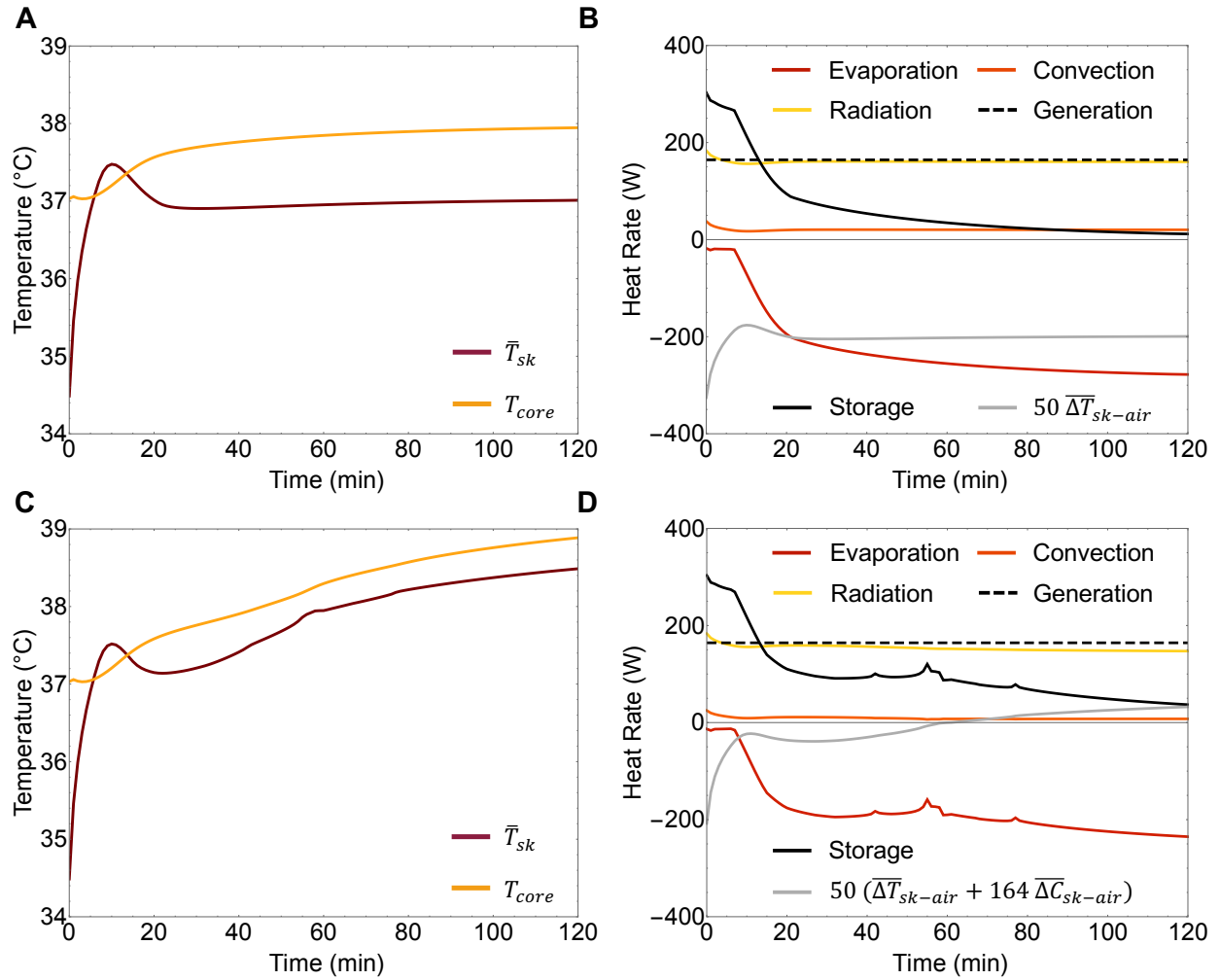


**Fig. 4. Thermophysiological responses predicted by the classical and coupled buoyancy effects included in updated Stolwijk thermoregulation model.** Simulations were performed for a lightly dressed (0.25 clo) young male with minimal activity (1.5 Met) inside a semi-outdoor canopy-covered tent with air at 41 °C and 20% RH, mean radiant temperature of 55 °C, and air velocity under 0.2 m·s<sup>-1</sup> over a 2 h exposure. Evolution of **(A)** mean skin temperature ( $\bar{T}_{sk}$ , °C), core temperature ( $T_{core}$ , °C), and **(B)** associated heat rates (W) (free convective, radiative, evaporative, metabolic heat generation and heat storage) predicted by the temperature difference based classical Stolwijk model (10). **(C, D)** Corresponding predictions from the updated physics-informed Stolwijk model incorporating the combined temperature- and humidity-difference driven buoyancy effects. **(B,D)** For visualization, the buoyancy-driving terms for each model ( $\bar{\Delta T}_{sk-air}$  vs  $\bar{\Delta T}_{sk-air} + 164\bar{\Delta C}_{sk-air}$ ) are scaled by a factor of 50.  $\Delta T_{sk-air}$  (°C) and  $\Delta C_{sk-air}$  (kg·m<sup>-3</sup>) are the skin-to-air temperature and concentration differences respectively.



**Table 1.** Summary of empirical coefficients for the free convection correlations (Eq. 8) fitted for all body segments under positive and negative buoyancy regimes.  $h_0$  (diffusion-only term,  $W \cdot m^{-2} \cdot K^{-1}$ ) and B are fitted parameters,  $\sigma_{h_0}$  and  $\sigma_B$  are their standard errors, respectively, and  $R^2$  is the coefficient of determination.  $\Delta T_{sk-air}$  ( $^{\circ}C$ ) and  $\Delta C_{sk-air}$  ( $kg \cdot m^{-3}$ ) are the skin-to-air temperature and concentration differences, respectively.

Segment	$\Delta T_{sk-air} + 164 \Delta C_{sk-air} > 0$					$\Delta T_{sk-air} + 164 \Delta C_{sk-air} < 0$				
	$h_0$	B	$\sigma_{h_0}$	$\sigma_B$	$R^2$	$h_0$	B	$\sigma_{h_0}$	$\sigma_B$	$R^2$
Head	0.470	1.076	0.038	0.024	0.999	0.470	1.509	0.038	0.015	0.997
Chest	0.144	0.991	0.026	0.016	0.999	0.144	1.212	0.026	0.016	0.995
Back	0.167	0.972	0.026	0.016	0.999	0.167	1.267	0.026	0.015	0.997
Whole torso	0.202	1.030	0.025	0.016	0.997	0.202	1.120	0.025	0.013	0.996
Upper Arm	0.742	1.205	0.028	0.017	0.999	0.742	1.304	0.028	0.021	0.995
Forearm	0.969	1.597	0.029	0.018	0.999	0.969	1.255	0.029	0.020	0.996
Whole arm	0.814	1.328	0.028	0.017	0.999	0.814	1.288	0.028	0.020	0.996
Pelvis	0.264	1.100	0.024	0.015	0.999	0.264	0.967	0.024	0.012	0.996
Thigh	0.430	1.210	0.025	0.015	0.999	0.430	0.749	0.025	0.013	0.994
Calf	0.480	1.345	0.019	0.012	0.999	0.480	0.704	0.019	0.010	0.996
Whole leg	0.457	1.283	0.022	0.135	0.999	0.457	0.725	0.022	0.020	0.995
Foot	0.966	1.756	0.026	0.016	0.999	0.966	0.991	0.026	0.021	0.994

**Table 2.** Summary of regional free convective coefficients ( $h_c$ ,  $W \cdot m^{-2} \cdot K^{-1}$ ) used across various modeling approaches namely Stolwijk (10, 27), JOS-2 & JOS-3 (33, 47), Wissler (7) and present study (Eq. 8).  $N = \Delta T_{sk-air} + 164\Delta C_{sk-air}$ , where  $N$  is the coupled buoyancy driving term,  $h_0$  (diffusion-only term,  $W \cdot m^{-2} \cdot K^{-1}$ ) and  $B$  are fitted parameters,  $\Delta T_{sk-air}$  ( $^{\circ}C$ ) and  $\Delta C_{sk-air}$  ( $kg \cdot m^{-3}$ ) are the skin-to-air temperature and concentration differences respectively (see SI Appendix, Text S6 for details)

<b>Model</b>	<b>Stolwijk</b> (10, 27)	<b>JOS-2, JOS-3</b> (33, 47)	<b>Wissler (7)</b> $h_c = A(\Delta T_{sk-air})^{1/4}$	<b>Present study</b> $h_c = h_0 + B \Delta T_{sk-air} + 164\Delta C_{sk-air} ^{1/4}$		
<b>Zone</b>	$h_c$	$h_c$	$A$	$h_0$	$B (N > 0)$	$B (N < 0)$
Head	0.660	4.480	2.600	0.470	1.076	1.509
Torso	1.860	2.910	1.500	0.202	1.030	1.120
Arms	3.950	3.590	1.900	0.814	1.328	1.255
Hands	6.050	3.670	2.700	0.500	2.400	2.400
Legs	3.610	2.530	2.150	0.457	1.283	0.725
Feet	5.930	2.040	1.570	0.969	1.756	0.991

## Supporting Information for

### Humidity lightens the air—but hinders human evaporative cooling in arid heat.

Shri H. Viswanathan, Ankit Joshi, Isabella DeClair, Bryce Twidwell, Muhammad Abdullah, Lyle Bartels, Faisal Abedin, Joseph Rotella, Cibin T. Jose, and Konrad Rykaczewski

Konrad Rykaczewski  
Email: [konradr@asu.edu](mailto:konradr@asu.edu)

#### **This PDF file includes:**

Supporting text S1 to S6  
Figures S1 to S19  
Tables S1 to S4  
SI References

## Supporting Information - Text S1

### 1. Chilton-Colburn analogy and Lewis relationship

During simultaneous heat (convection) and mass (sweat evaporation) transfer, the transport processes are analogous and the convective heat ( $h_c$ ,  $W \cdot m^{-2} \cdot K^{-1}$ ) and mass ( $h_{mass}$ ,  $m \cdot s^{-1}$ ) transfer coefficients are related through the Chilton-Colburn analogy (**Eq. S1**) (for  $0.6 < Pr < 60$  and  $0.6 < Sc < 3000$ ), where the Lewis number ( $Le = \alpha/D = k/(\rho c_p D)$ , dimensionless, (1)) is defined as the ratio of thermal ( $\alpha$ ,  $m^2 \cdot s^{-1}$ ) to mass diffusivity ( $D$ ,  $m^2 \cdot s^{-1}$ ),  $k$ —thermal conductivity of air ( $W \cdot m^{-1} \cdot K^{-1}$ ),  $\rho$ —air density ( $kg \cdot m^{-3}$ ),  $c_p$ —specific heat at constant pressure ( $J \cdot kg^{-1} \cdot K^{-1}$ ). **Eq. S2 & S3** describe the mass flux rate of sweat evaporated ( $\dot{m}$ ,  $kg \cdot m^{-2} \cdot s^{-1}$ ) and evaporative heat flux ( $Q_e$ ,  $W \cdot m^{-2}$ ), where  $\lambda$  is the latent heat of vaporization ( $J \cdot kg^{-1}$ ),  $p$ —atmospheric pressure (Pa),  $M_v$  &  $M_{air}$ —molar masses of water vapor and moist air mixture respectively ( $kg \cdot mol^{-1}$ ),  $p_{sk}$  &  $p_{air}$ —vapor pressures at the skin surface and ambient air respectively (kPa). Substituting **Eq. S1 & S2** into **Eq. S3** gives **Eq. S4**. The terms within the square brackets are grouped together and evaluated at air temperature of 25 °C (the air properties variation has minimally impact on the calculations across the 20–50 °C range), and skin temperature of 32 °C (2), forming the Lewis relationship ( $LR = 16.5 K \cdot kPa^{-1}$ ) (**Eq. S5**). Finally, the evaporative transfer coefficient ( $h_e$ ,  $W \cdot m^{-2} \cdot kPa^{-1}$ ) is expressed as a function of the Lewis relationship (3) and the convective heat transfer coefficient (**Eq. S6**).

$$\frac{h_c}{h_{mass}} = \rho c_p Le^{2/3} \quad [S1]$$

$$\dot{m} = \frac{h_{mass} \rho}{p} \frac{M_v}{M_{air}} (p_{sk} - p_{air}) \quad [S2]$$

$$Q_e = \dot{m} \lambda \quad [S3]$$

$$Q_e = \left[ \frac{\lambda}{\rho c_p Le^{2/3}} \frac{M_v}{M_{air}} \right] h_c (p_{sk} - p_{air}) \quad [S4]$$

$$Q_e = LR h_c (p_{sk} - p_{air}) = 16.5 h_c (p_{sk} - p_{air}) = h_e (p_{sk} - p_{air}) \quad [S5]$$

$$h_e = 16.5 h_c \quad [S6]$$

## Supporting Information - Text S2

### 2. Experimental verification of the Lewis relationship under forced convective conditions

Controlled experiments were conducted within a climate-controlled wind enclosure using a thermal manikin (**Fig. S1A–F**) and the experimentally measured evaporative coefficients were compared against the Lewis factor ( $16.5 K \cdot kPa^{-1}$ , **Eq. S6**) scaled dry forced convective coefficient.

#### 2.1 Wind Enclosure

A custom wind enclosure (3.5 m length, 1.14 m width, 2.28 m height) was built within a climatic chamber (6 m length, 2.75 m width, 3 m height) (**Fig. S1C**) using T-slot aluminum extrusions and polycarbonate panels (4, 5). To simplify the computational estimation of radiative heat transfer, the enclosure's inner walls, ceiling and floor were covered with highly emissive black kraft paper with a longwave emissivity of 0.99 (measured using a PerkinElmer Frontier Fourier Transform Infrared Spectrometer (FTIR) (4, 6)). To ensure a horizontal homogenous airflow with low turbulence, air was pulled across the enclosure by three fans (XPOWER FD-630D, 0.61 m diameter) through a 6 cm thick polycarbonate honeycomb panel (manufactured by Plascore, Inc., 6 mm pores) at the entrance (**Fig. S1D**). The mean upstream air speed ( $v_{air}$ ) was measured across five locations using five omnidirectional hot wire anemometers (**Fig. S1E**). Moreover, the inlet air temperature ( $T_{air}$ ), and relative humidity ( $RH_{air}$ ) (**Fig. S1F**) were also measured using the instruments outlined in **Table S1**.

#### 2.2 Thermal manikin – ANDI

To investigate the heat and moisture transport around the human body, experiments were conducted using a custom-built thermal manikin, "Advanced Newton Dynamic Instrument" (ANDI) developed by Thermetrics, LLC (Seattle, USA). ANDI (**Fig. S1A–B**) represents a 50<sup>th</sup> percentile western male, standing 1.78 m tall with a total surface area of 1.86 m<sup>2</sup>. The manikin consists of 35 independently controlled segments, each with area-distributed resistive temperature sensors embedded beneath the surface (4, 5, 7, 8). ANDI was placed inside the enclosure and was mounted on a non-reflective mobile

stand at its lower back. The actuated joints of ANDI's limbs were covered with masking tape to prevent the air flow from entering the hollow manikin shell (4). The manikin's surface can be operated in either constant uniform skin temperature ( $T_{sk}$ ) or heat flux mode. The former is more replicative of the human skin in a thermally neutral environment (3, 9). Moreover, this method averts the complications of inter-segment radiation which would otherwise occur during constant uniform heat flux mode (4) due to non-uniform skin temperature.

While legacy thermal manikins are designed solely to quantify heat loss into the surroundings, ANDI's area-distributed differential heat flux sensors, embedded beneath the surface, can measure both heat loss to and gain from the surroundings. Additionally, the internal cooling channels present under the surface absorb the excess incoming heat, preventing the manikin skin temperature ( $T_{sk}$ ) from exceeding its setpoint (7, 8). These capabilities enable its utility in both hot and cold environments. Furthermore, ANDI replicates the human sweat evaporation process through its 151-flow rate controlled sweat pores spread evenly across the body. To achieve a uniform moisture dispersion across the surface, the manikin was dressed in an artificial textile "skin" (sweat wicking polyester onesie, 0.5 mm thick). Excess water runoff from the manikin was collected in a tray placed beneath the feet. To prevent water evaporating from the tray and disrupting the manikin measurements, a thin layer of oil was applied to water surface.

### 2.3 Experimental procedure

To verify the applicability of the Lewis relationship under forced convective conditions, two complementary sets of experiments were conducted using the thermal manikin present within the wind enclosure. For each set, five different air speed settings were chosen between 0.34 and 1.71 m·s<sup>-1</sup>. Firstly, to isolate the sensible-heat exchange and estimate the dry forced convective heat transfer coefficient ( $h_{dry}$ , W·m<sup>-2</sup>·K<sup>-1</sup>), the manikin surface was maintained dry at constant uniform temperature of 35 °C, while the inlet air was held at 22.9 ± 0.1 °C and 37.9 ± 1.2% RH.

Secondly, to eliminate sensible heat exchange and isolate the latent-heat exchange (only velocity driven mass transfer at constant  $RH_{air}$  i.e., sweat evaporation),  $T_{sk}$  and  $T_{air}$  were maintained at 35 °C (isothermal conditions). The manikin was dressed in its water-saturated textile "skin", while  $RH_{air}$  was held at 49.4 ± 5.5 % RH. The wet textile "skin" was characterized to offer a thermal resistance ( $R_{txt}$ , Inset of **Fig. S2**) of 0.0054 m<sup>2</sup>·K·W<sup>-1</sup>. During experimentation, all the enclosure walls were nearly in equilibrium with  $T_{air}$ . Once the enclosure's thermal environment stabilized, all zonal manikin parameters (e.g., skin temperature, heat flux etc.) were recorded every 5 s. All 10 cases were repeated thrice leading to 30 trials, where each trial lasted 75 minutes. During the final 30 minutes, the segmental skin temperature fluctuations remained under 0.05 °C, indicating steady state condition. We note that under the low heat fluxes occurring during free convection, the textile skin thermal resistance has negligible impacts.

### 2.4 Experimental results

The whole-body total heat flux ( $Q_{Total}$ , W·m<sup>-2</sup>) was computed by segmental area weighting of the zonal-time average data collected during steady state. Specifically for the dry forced convection trials, the computationally estimated whole-body radiative heat flux (60.1 W·m<sup>-2</sup>) was subtracted from  $Q_{Total}$ , and the remainder was divided by the skin-to-air temperature gradient, to yield the dry forced convective heat transfer coefficient ( $h_{dry}$ , W·m<sup>-2</sup>·K<sup>-1</sup>). To obtain its evaporative-equivalent,  $h_{dry}$  was multiplied by the Lewis factor (16.5 K·kPa<sup>-1</sup>, **Eq. S6**). On other hand, for the isothermal velocity driven mass transfer experiments, the total heat flux ( $Q_{Total}$ ) corresponds only to the evaporative heat losses ( $Q_e$ ) from the manikin. Accounting for the textile skin's thermal resistance, there exists a significant temperature drop between manikin surface ( $T_{sk}$ ) and textile "skin" ( $T_{txt}$ ). So  $Q_e$  was divided by the textile-to-air vapor pressure gradient ( $p_{txt|T_{txt}} - p_{air|T_{air}}$ ) (Inset of **Fig. S2**) to obtain the corrected evaporative heat transfer coefficient ( $h_{exp}$ , W·m<sup>-2</sup>·kPa<sup>-1</sup>).

As illustrated in **Fig. S2**, there exists a strong agreement between the evaporative equivalent of  $h_{dry}$  and  $h_{exp}$  across the tested air speed range, thus experimentally demonstrating the validity of the Lewis relationship under forced convective conditions. Furthermore, the evaporative equivalent of the empirical dry forced convective coefficient proposed by Joshi et al. (7) aligned closely with our experimental results. In contrast, the evaporative coefficients (uncorrected  $h_{exp}$ , W·m<sup>-2</sup>·kPa<sup>-1</sup>) computed without considering the textile skin's resistance ( $Q_e$  directly divided by skin-to-air vapor pressure gradient ( $p_{sk|T_{sk}} - p_{air|T_{air}}$ )) were consistently lower than  $h_{exp}$  across the entire test range, highlighting the importance of including the manikin's textile "skin" resistance in evaporative flux measurements.

## Supporting Information - Text S3

### 3. Experimental validation of the coupled free convection, sweat evaporation and radiation model using thermal manikin

This section presents the experimental validation of the coupled free convection, evaporation and radiation model using the sweating thermal manikin ANDI. We conducted controlled experiments inside a sealed enclosure under a range of temperature and humidity conditions and replicated these cases using multiphysics simulations. The measured whole-body total heat fluxes closely matched the simulations, confirming the model's reliability across diverse conditions.

#### 3.1 Sealed enclosure

Controlled experiments were conducted inside a sealed enclosure located within a climatic chamber (**Fig. S3A–F**) as previously described in **SI Appendix, Text S2**. To study free convection within the enclosure, we ensured the air speed within the enclosure was less than  $0.02 \text{ m}\cdot\text{s}^{-1}$  by completely sealing the enclosure (including the honeycomb entrance wall and fan wall) (**Fig. S3D**) with highly emissive black kraft paper. Moreover, the black kraft paper also simplified the computational estimation of radiative heat transfer. Additionally, a chimney (0.81 m length, 1.14 m width, 0.31 m height) was integrated into the enclosure to function either as an inlet for fresh air from the chamber or an outlet for the rising thermal plume, depending on the thermal conditions and the resulting buoyancy-driven flow (4). The instrumentation used within the enclosure to measure the air temperature ( $T_{air}$ ), relative humidity ( $RH_{air}$ ), air speed ( $v_{air}$ ) and wall temperature ( $T_{wall}$ ) (**Fig. S3A–E**) are outlined in **Table S2**.

#### 3.2 Experimental procedure

We conducted a comprehensive set of experiments under controlled conditions (15 cases) as listed in **Table S3**, to generate buoyant flow near the skin driven by temperature-only, humidity-only, and combined temperature-humidity effects. Each case was repeated thrice to demonstrate reproducibility, resulting in 45 trials. Before each run, the thermal manikin (as described in **SI Appendix, Text S2**) was positioned beneath the chimney, and the enclosure was sealed. The air speed ( $v_{air}$ ) (**Fig. S3B**) within the enclosure remained under  $0.02 \text{ m}\cdot\text{s}^{-1}$ , indicating conditions suitable for investigating free convection.

To isolate temperature-only driven free convection (cases 1–4), the manikin surface was held dry (**Fig. S3F**).  $T_{air}$  was varied between 40.3 and 44.8 °C at constant absolute humidity (12.55 g of water per kg of dry air). Here, the heat flux measured by the manikin corresponds only to free convective and radiative heat gain from the environment ( $T_{air} > T_{sk}$ ). To isolate humidity-only driven sweat evaporation (cases 5–8), both the manikin surface and surrounding air were isothermally held at 35 °C, while  $RH_{air}$  was varied between 35.6 and 81.4%. To enable a uniform moisture dispersion across the manikin surface, replicative of the human skin, the manikin was covered with the water-saturated (at 35 °C) textile “skin” (**Fig. S3F**). Finally, the combined effects of temperature and humidity were examined in cases 9-15 by maintaining  $T_{air}$  4.6 °C or 7.5 °C above  $T_{sk}$ , meanwhile varying  $RH_{air}$ .

Once the enclosure's thermal environment stabilized, the manikin was switched on, and its zonal parameters (e.g., skin temperature, heat flux etc.) were recorded every 5 s. Each run lasted 75 minutes, with segmental skin temperature fluctuations remained under 0.05 °C during the final 30 minutes, indicating steady state condition. The far-field air temperature ( $T_{air}$ ) (**Fig. S3C**) measured within the sealed enclosure was used for analysis and was consistently 0.1 to 1.6 °C lower than the chamber setpoints ( $T_c$ , °C). For each trial, the whole-body total heat flux ( $Q_{Exp-WB}$ ,  $\text{W}\cdot\text{m}^{-2}$ ) was computed by segmental area weighting of the zonal-time average data collected during steady state.

The Type A (experimental) uncertainty ( $u_A$ ) and Type B (instrumental) uncertainty ( $u_B$ ) were estimated for each zonal total heat fluxes ( $Q_{Exp-z}$ ) and combined to determine the total standard uncertainty ( $u_C$ ). A coverage factor ( $k$ ) was multiplied to  $u_C$  to expand the uncertainty to form the overall uncertainty ( $U$ ) (**Eq. S7**). For a two-tailed Student's  $t$ -distribution with 2 degrees of freedom, 3 repetitions, 95% confident level,  $k$  was 4.303.

$$U = ku_C = k\sqrt{(u_A^2 + u_B^2)} \quad \text{[S7]}$$

### 3.3 Coupled radiative, flow, moisture and heat transfer simulation

A multiphysics computational model was developed in COMSOL Multiphysics 6.3 (finite element-based software) to quantify coupled heat and mass transfer around the thermal manikin and validate the whole-body and zonal heat fluxes against experimental measurements. The experimental sealed enclosure was geometrically replicated and a water-tight surface mesh of the thermal manikin, used in our prior work (4), was imported into the virtual enclosure as shown in **Fig. S4A**. The virtual manikin closely matched its physical counterpart with its total surface mesh area differing only by 1.7% from the actual manikin. To reduce the computational time, symmetry conditions were applied for the entire geometry along the sagittal/median plane.

The numerical model solves for various physics modules namely, “Fluid Flow” (Low Re  $k$ - $\epsilon$  Turbulence model with Low Re wall functions), “Moisture Transport”, “Heat transfer in fluids” and “Surface-to-Surface Radiation”. These modules were coupled together through “Non-Isothermal flow”, “Heat transfer with surface-to-surface radiation”, “Heat and moisture flow”, and “Moisture flow” multiphysics modules. Moist air was chosen as the fluid medium, and gravity was enabled to account for the buoyancy effect. A weakly compressible flow was assumed to simulate the buoyancy generated due to moisture concentration and temperature gradients (density variations induced by fluid pressure gradients were neglected). For cases 1 to 4 and 9 to 15, since  $T_{air} > T_{sk}$ , a downward plume was established by drawing fresh air into the enclosure from the chamber through the chimney. Accordingly, the chimney’s top surface served as the inlet, with a velocity of  $0.02 \text{ m}\cdot\text{s}^{-1}$  (5% turbulence intensity and geometry based turbulence length scale) and thermal conditions identical to those of the chamber ( $T_c$  &  $RH_c$ , **Table S3**), while the entire enclosure floor served as the outlet. In contrary, for cases 5 to 8, the inlet and outlet boundaries were interchanged, due the upward plume ( $T_{air} < T_{sk}$ ).

All the model reference values were computed at  $T_{air}$  &  $RH_{air}$ , representative of the thermal conditions within the enclosure measured far from the manikin. The virtual manikin’s surface temperature was set to  $T_{sk}$  from **Table S3**. While simulating the isothermal cases 5-8 and the combined heat and mass transfer experiments (Cases 9-15), the evaporative rate parameter of the virtual manikin’s surface was set to  $100 \text{ m}\cdot\text{s}^{-1}$ , representative of fully wet surface. The enclosure’s humidity was set to  $RH_{air}$  from **Table S3**. The radiative heat exchange was computed using surface-to-surface radiation method (hemicube technique with resolution of 64). Since all the surfaces were assumed to be diffuse and gray, the surface radiative properties were set to “wavelength independent”. The emissivity of the enclosure and the manikin surface were set to 0.99 and 0.98 respectively. Since  $T_{air}$  was consistently cooler than  $T_c$ , to model the heat gained by the enclosure from the chamber, an effective heat transfer coefficient of  $5.6 \text{ W}\cdot\text{m}^{-2}\cdot\text{K}^{-1}$  was applied on the enclosure walls (4). Unlike in **SI Appendix, Text S2**, where accounting for the textile skin’s thermal resistance was crucial in the evaporative heat loss calculations, it was neglected and not modelled computationally in cases 5-15 because the measured  $Q_{Exp-WB}$  were small, leading to a negligible temperature difference ( $T_{sk} - T_{txt} < 0.5 \text{ }^\circ\text{C}$ ) between the manikin surface and the textile skin.

The entire enclosure was meshed using free triangular cells for the floor and prism elements for the remaining volume. Two high-density cuboidal mesh volumes (refinement zones) were added around the manikin to accurately resolve the velocity, temperature and moisture gradients near the manikin surface. **Fig. S4B** demonstrates the mesh refinement study that was conducted to determine when the free convective heat transfer coefficient and total heat flux becomes independent of the number of mesh elements. The final mesh contained 507510 elements with a maximum element size of 7.2 cm, a minimum element size of 1.6 cm, an element growth rate of 1.14, a curvature factor of 0.5, and a resolution of narrow region of 0.8. Following the COMSOL Multiphysics software’s recommendations (10), the “distance to the cell center in viscous units” was maintained below 0.5 by applying 15 boundary layers, stretching factor of 1.2, and a total boundary layer thickness of 1 cm. The average element quality was 0.76. Following meshing, the model was initialized using a wall distance step and solved with a time-dependent study over 300 s. A quasi-steady state was reached between 240 and 300 s, with net heat flux variations under 5%. Time-averaged free convective, radiative and evaporative heat fluxes were computed to estimate the total heat flux ( $Q_{Sim-WB}$ ,  $\text{W}\cdot\text{m}^{-2}$ ) which was benchmarked against the experimental measurements.

### 3.4 Experimental validation of the multiphysics model

**Fig. S5A–D** compares whole-body and zonal total heat fluxes measured experimentally and estimated by simulations for all the 15 cases. Overall, the multiphysics model closely agrees with the experimental measurements, with simulated total heat fluxes generally within the experimental uncertainties. In cases 7, 9 & 13, the model underestimates the experimental heat fluxes by up to 23%,

slightly exceeding the uncertainty bounds. To facilitate regional comparison, ANDI's 35 zones were grouped into 12 larger anatomical regions by area-weighted summation. Hands and feet were excluded from the analysis for several reasons. In particular, for cases 5–15, excess sweat from other zones accumulated on the fingers and feet and dripped into the water tray present below, which was not modeled in the simulations. In addition, only the manikin's palmar regions were heated and sweating, while the fingers were passive, hence hands were excluded.

**Fig. S6A–D** shows strong overall agreement between experimental ( $Q_{Exp-z}$ ,  $W \cdot m^{-2}$ ) and simulated ( $Q_{Sim-z}$ ,  $W \cdot m^{-2}$ ) zonal total heat fluxes. In particular, the head, back torso, upper arms, forearms, thighs, and calves exhibit good consistency, with simulated values falling within experimental uncertainties in at least 60% of cases. Minor discrepancies in the aforementioned regions are primarily attributable to simplified geometry of local zones and the partially loose fit of the manikin's textile skin (sweat wicking garment). For instance, simulated fluxes for the upper arms, forearms, thighs and calves agree with experiments in 68.3% of cases, with average deviations of only 10.1%, 14.1%, 9.5% and 13.3% respectively. Minor discrepancies arise in the remaining cases because the physical manikin has passive actuated joints around the elbows and kneecaps that are unheated and lack sweat pores, whereas the virtual model simplifies these regions as one continuous heated wet surface. For the back torso, simulations matched experimental values in 10 of 15 cases, with an average deviation of 12.9%. Discrepancies in the remaining cases likely arise from the unmodeled fixtures in the lower back—such as the mobile stand attachment, cooling water lines, and communication cables—that disrupt the local buoyant plume. This plume disruption also affected the pelvis region, where additional factors amplified the average deviations to 18.3% from experimental values. Particularly, a passive insulated joint along the sagittal plane, designed to support leg movement, was geometrically simplified in the virtual model as an actively heated, wet surface. Furthermore, the textile “skin” was loosely fitted near the crotch, creating air gaps that altered local heat fluxes.

Simulated total heat fluxes for the head closely matched experimental measurements for 10 of 15 cases, with an average deviation of 11.9%. These discrepancies were primarily due to the manikin's crown that comprises of a passive hollow shell intended for occasional attachment to the mobile stand, and partial coverage of the head and neck by the textile skin's zipper. In cases 9–12, nearly 70% of the head remained partially dry due to clogged sweat pores, reducing evaporation and total heat flux experimentally. After unclogging the pores, the head was maintained fully wet in cases 13–15, resulting in closer agreement with simulations. For the front torso, simulated total heat fluxes deviated on average by 22.1% from experimental measurements. The largest contributor to this discrepancy was the simplified armpit geometry in the model, whereas the physical manikin features a passive actuated upper arm–shoulder joint that was not represented computationally. Additional factors included the loosely fitting textile “skin” around the armpit, which occasionally produced partially dry patches in the pectoral and underarm regions, further affecting local heat fluxes.

Additionally, the wall temperature at the location shown in **Fig. S3A** and the air speed measured above the manikin's head (**Fig. S3E**) exhibited good agreement with the corresponding simulated values, as illustrated in **Fig. S7A–D**, further supporting the validity of the numerical model.

## Supporting Information - Text S4

### 4.1 Experimentally validated multiphysics model setup for parametric study

The parametric study was performed in a simplified virtual enclosure (4 m length, 2 m width, 3 m height) (**Fig. S8A**). A 3D watertight geometry of a western average male (50<sup>th</sup> percentile height (m) and BMI ( $kg \cdot m^{-2}$ )) was positioned at the geometric center of the enclosure (**Fig. S8B**). Since the entire geometry was symmetrical, only one-half of the geometry was simulated, to reduce the computational cost. The model consisted of “Turbulent Fluid Flow”, “Heat Transfer in Fluids”, and “Moisture Transport” physics modules and were interlinked through “Non-Isothermal flow”, “Heat and Moisture Transfer” and “Moisture flow” multiphysics couplings. A Low-Re  $k-\epsilon$  Turbulence model (Low-Re wall functions) was used to accurately resolve the flow features near the skin surface. A weakly compressible flow of moist air was assumed, and the gravity module was enabled to capture the buoyancy-driven flow. The skin was maintained at a constant temperature of 35 °C and modeled as a saturated wet surface. To prevent numerical convergence issues, the inlet and outlet boundaries of the enclosure were dynamically assigned based on the natural flow



direction. For cases with an ascending buoyant plume, the floor served as the inlet and the ceiling as the outlet and vice versa for a descending plume. The inlet  $T_{air}$  and  $RH_{air}$  were parametrically varied between 20–50 °C and 10–90% respectively.

The entire geometry was discretized using free triangular elements for the floor and prism elements in the remaining volume. Two high-density cuboidal mesh volumes were generated around the body to accurately capture the steep velocity, temperature and moisture gradients near the skin surface. A mesh refinement study was conducted to identify when the free convective coefficient ( $h_{sim}$ ,  $W \cdot m^{-2} \cdot K^{-1}$ ) became independent of mesh density (**Fig. S8C**). The final optimized mesh contained 370576 elements with a maximum and minimum element size of 7.5 and 2 cm respectively, an element growth rate of 1.13, a curvature factor of 0.5, and a narrow region resolution of 0.8. The "distance to the cell center in viscous units" was maintained below 0.5 by applying 15 boundary layers, stretching factor of 1.2, and a total boundary layer thickness of 2 cm, resulting in an average element quality of 0.75. The model was initialized with a wall distance method and solved in a transient study (50 s) to compute the free convective heat transfer coefficients ( $h_{sim}$ ) and evaporative heat losses ( $Q_{sim}$ ,  $W \cdot m^{-2}$ ). The variation in  $h_{sim}$  decreased by less than 2% after 30 s, indicating that quasi-steady state had been achieved.

#### 4.2 Buoyancy forces induced by temperature- and humidity-differences

The individual buoyant forces arising from the temperature ( $\Delta T_{sk-air} = T_{sk} - T_{air}$ ) and humidity or moisture concentration differences ( $\Delta C_{sk-air} = C_{sk} - C_{air}$ ), namely,  $B_{\Delta T} = g\rho\beta_T\Delta T_{sk-air}$  and  $B_{\Delta C} = g\rho\beta_C\Delta C_{sk-air}$ , were computed, where  $g$  is the gravitational acceleration ( $9.81 \text{ m} \cdot \text{s}^{-2}$ ),  $\beta_T$  is the thermal coefficient of expansion (reciprocal of the absolute average of  $T_{air}$  and  $T_{sk}$ ), and  $\beta_C$  is the coefficient of expansion due to compositional changes.  $\beta_C$  can be obtained from the density of air ( $\rho$ ), the average molecular weight of air ( $MW_a = 29 \text{ g} \cdot \text{mol}^{-1}$ ), and that of water vapor ( $MW_c = 18.02 \text{ g} \cdot \text{mol}^{-1}$ ) as  $(MW_a/MW_c - 1)/\rho$  or  $0.607/\rho$  (11). **Table S4** outlines the behavior of  $B_{\Delta T}$ ,  $B_{\Delta C}$  and the net buoyancy  $B_{Net}$ —which is the sum of both buoyancies—across various air temperature regimes.  $B_{\Delta T}$ ,  $B_{\Delta C}$  and  $B_{Net}$  are computed and plotted as function of skin-to-air temperature differences for each  $RH_{air}$  as shown in **Fig. S9A–C**, **Fig. S10A–C**, and **Fig. S11A–C**

#### 4.3 Coupled temperature and humidity impact on free convection and sweat evaporation

Using the experimentally validated multiphysics model, we systematically varied the  $T_{air}$  (20–50 °C) and  $RH_{air}$  (10–90%) (100 cases total using Research Computing at Arizona State University (12)) to investigate the coupled impact of thermal- and humidity-gradients on whole-body free convective coefficients ( $h_{sim}$ ,  $W \cdot m^{-2} \cdot K^{-1}$ ) and evaporative heat fluxes ( $Q_{sim}$ ,  $W \cdot m^{-2}$ ), for an average western male (50<sup>th</sup> percentile BMI and height), while maintaining a water-saturated skin surface at 35 °C. **Fig. S12A–F**, **Fig. S13A–F**, and **Fig. S14A–F** compare the simulated values against the widely used empirical correlations that are solely a function of the skin-to-air temperature-differences.

$$h_{\Delta T-only} = 1.36 |\Delta T_{sk-air}|^{0.3} \quad [\text{S8}]$$

$$Q_{\Delta T-only} = 16.5 h_{\Delta T-only} \Delta p_{sk-air} \quad [\text{S9}]$$

Where,  $h_{\Delta T-only}$  ( $W \cdot m^{-2} \cdot K^{-1}$ ) is the empirical whole-body dry free convective heat transfer coefficient correlation derived from our prior studies ( $T_{sk} > T_{air}$ , (4)) and validation cases 1–4 as described in **SI Appendix, Text S3**.  $Q_{\Delta T-only}$  ( $W \cdot m^{-2}$ ) is the evaporative heat flux obtained as a function of the empirical dry free convective coefficient (**Eq. S8**), Lewis factor ( $16.5 \text{ K} \cdot \text{kPa}^{-1}$ , **Eq. S6**) and the skin-to-air vapor pressure differences ( $\Delta p_{sk-air} = p_{sk} - p_{air}$ ).

#### Supporting Information - Text S5

#### 5. Physics-based model for free convective coefficients accounting for humidity-induced buoyancy

$$h_c = h_0 + B |\Delta T_{sk-air} + 164 \Delta C_{sk-air}|^{1/4} \quad [\text{S10}]$$

Here,  $h_0$  is the diffusion-only value,  $B$  is the coefficient specifying geometrical, flow, and fluid property impacts, and  $\Delta T_{sk-air} + 164 \Delta C_{sk-air}$  is the combined temperature and concentration buoyancy driving term.

Fitting this physics-informed model (Eq. S10) to individual body segments yields excellent agreement with simulation results (see Manuscript, Table 1 and Fig. S15A–F, Fig. S16A–F & Fig. S17A–F).

## Supporting Information - Text S6

### 6. Local free convective correlations for hands and feet

Simulated local convective coefficients ( $h_c$ ,  $W \cdot m^{-2} \cdot K^{-1}$ ) for hands were fitted using temperature-difference scaling (Eq. S11) and combined temperature- and concentration-difference scaling (Eq. S12) approaches and compared with average Quintela et al. correlations (13) (Eq. S13–S14) for hands across skin-to-air temperature differences for dry skin (i.e.,  $\Delta C_{sk-air} = 0$ ) (Fig. S18A). Similarly for feet, the fitted correlations using both approaches (Eq. S15–S16) were compared in Fig. S18B.

$$h_c = 2.7 \Delta T_{sk-air}^{1/4} \quad [S11]$$

$$h_c = 0.5 + 2.4 \Delta T_{sk-air}^{1/4} \quad [S12]$$

$$h_c = 1.58 \Delta T_{sk-air}^{0.51} \text{ (Left hand)} \quad [S13]$$

$$h_c = 3.55 \Delta T_{sk-air}^{0.11} \text{ (Right hand)} \quad [S14]$$

$$h_c = 1.57 \Delta T_{sk-air}^{1/4} \quad [S15]$$

$$h_c = 0.969 + 0.99 \Delta T_{sk-air}^{1/4} \quad [S16]$$

### Acknowledgments:

This research was supported by the National Science Foundation #2152468 # 2214152 awards, while the thermal manikin was funded by a National Science Foundation Major Research Instrumentation grant #2117917. The authors gratefully acknowledge Research Computing at Arizona State University for providing high-performance computing resources that have contributed to the research results reported within this paper. The authors gratefully acknowledge the use of spectroscopy equipment within the Eyring Center for Solid State Science at Arizona State University.

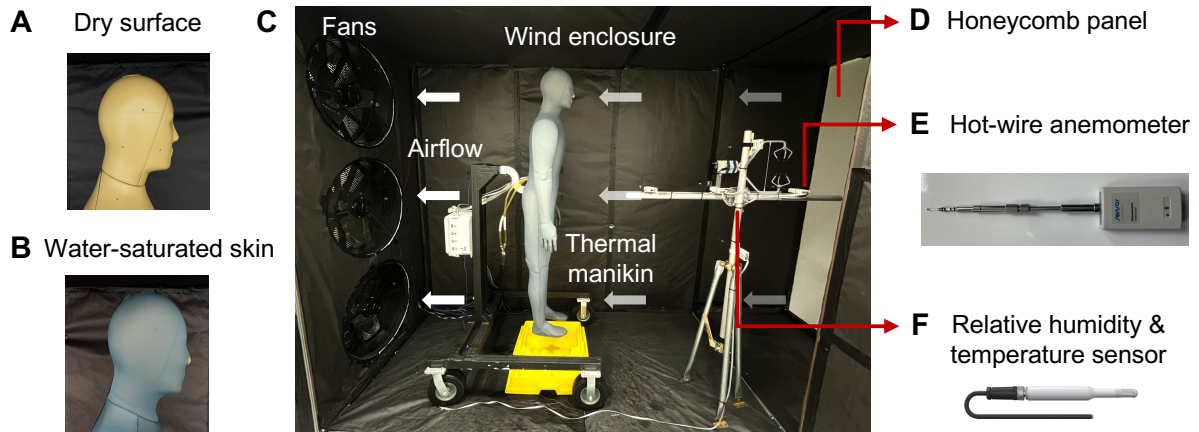


**Fig. S1. Forced convection experimental setup with the thermal manikin inside the wind enclosure.** (A) Dry manikin surface during sensible-heat exchange experiments, (B) Water-saturated textile skin worn by the manikin during latent-heat exchange experiments, (C–D) Airflow drawn through the honeycomb panel by the fans, (E) Five hot-wire anemometers (SensoAnemo 5100 LSF) and (F) Relative humidity and temperature sensor (EE181), as listed in **Table S1**.

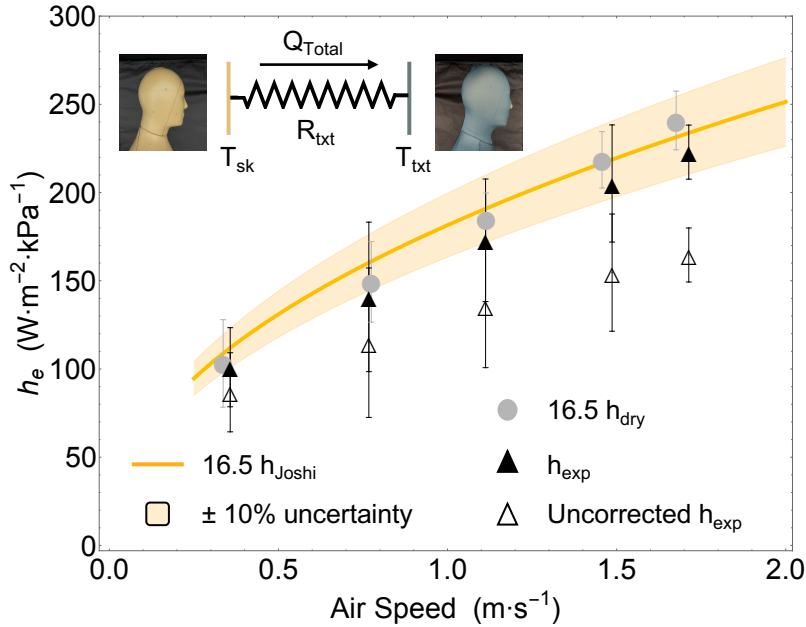


**Fig. S2. Comparison of measured and derived evaporative transfer coefficients and validating the applicability of Lewis relationship under forced convection.**  $h_e$  ( $\text{W}\cdot\text{m}^{-2}\cdot\text{kPa}^{-1}$ ) – evaporative heat transfer coefficient. The whole-body dry forced convective coefficients,  $h_{\text{dry}}$  ( $\text{W}\cdot\text{m}^{-2}\cdot\text{K}^{-1}$ ) and  $h_{\text{Joshi}}$  ( $\text{W}\cdot\text{m}^{-2}\cdot\text{K}^{-1}$ ) were obtained from (i) sensible-heat exchange experiments conducted inside the wind enclosure and (ii) empirical correlations of Joshi et al. (7), respectively. These dry coefficients were multiplied by the Lewis factor ( $16.5 \text{ K}\cdot\text{kPa}^{-1}$ ) to estimate their evaporative equivalents. The experimentally measured whole-body evaporative heat transfer coefficients,  $h_{\text{exp}}$  ( $\text{W}\cdot\text{m}^{-2}\cdot\text{kPa}^{-1}$ ), were determined from isothermal latent-heat exchange experiments after accounting for the manikin’s water-saturated textile skin’s thermal resistance ( $0.0054 \text{ m}^2\cdot\text{K}\cdot\text{W}^{-1}$ , see inset). The uncorrected  $h_{\text{exp}}$  ( $\text{W}\cdot\text{m}^{-2}\cdot\text{kPa}^{-1}$ ) computed without including textile’s thermal resistance, are also shown for comparison. The strong agreement between the evaporative equivalents of  $h_{\text{dry}}$ ,  $h_{\text{Joshi}}$  and  $h_{\text{exp}}$  across air speeds experimentally demonstrates the validity of the Lewis relationship under forced convective conditions. Experimental data points are averages of three replicates with 95% confidence intervals (combined Type A and B uncertainty).

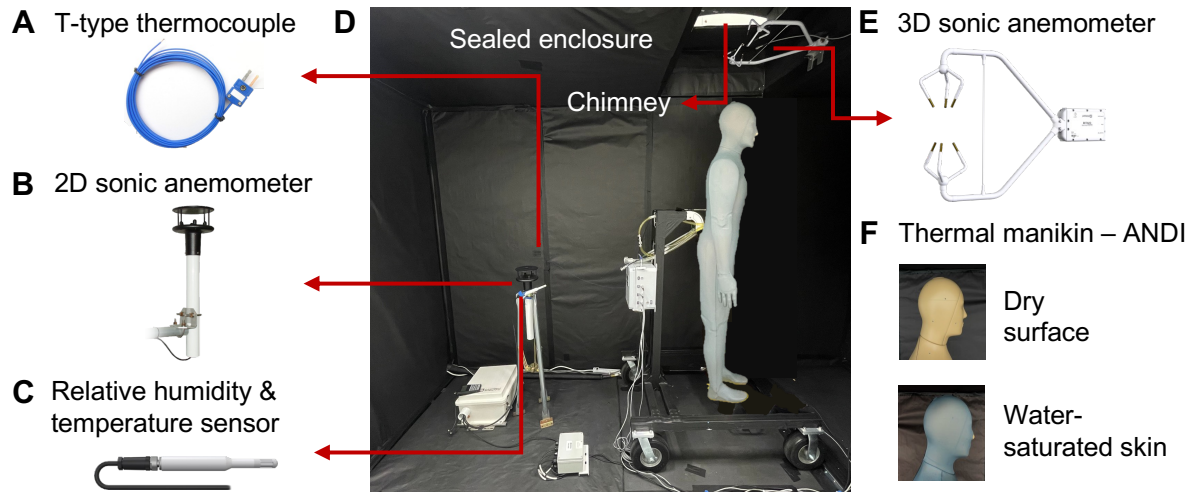


**Fig. S3. Free convection experimental setup with the thermal manikin inside the sealed enclosure.**

(A) T-type thermocouple measured the enclosure wall temperature, (B) 2D sonic anemometer (WINDSONIC1-L) and (C) Relative humidity and temperature sensor (EE181) measured the air speed, relative humidity and temperature within the (D) sealed enclosure respectively, (E) 3D sonic anemometer measured the air speed above the manikin's head. Instrumentation details are provided in **Table S2**. (F) Dry manikin surface used for temperature-only driven heat transfer experiments and water-saturated textile skin worn by the manikin for experiments involving sweat evaporation.

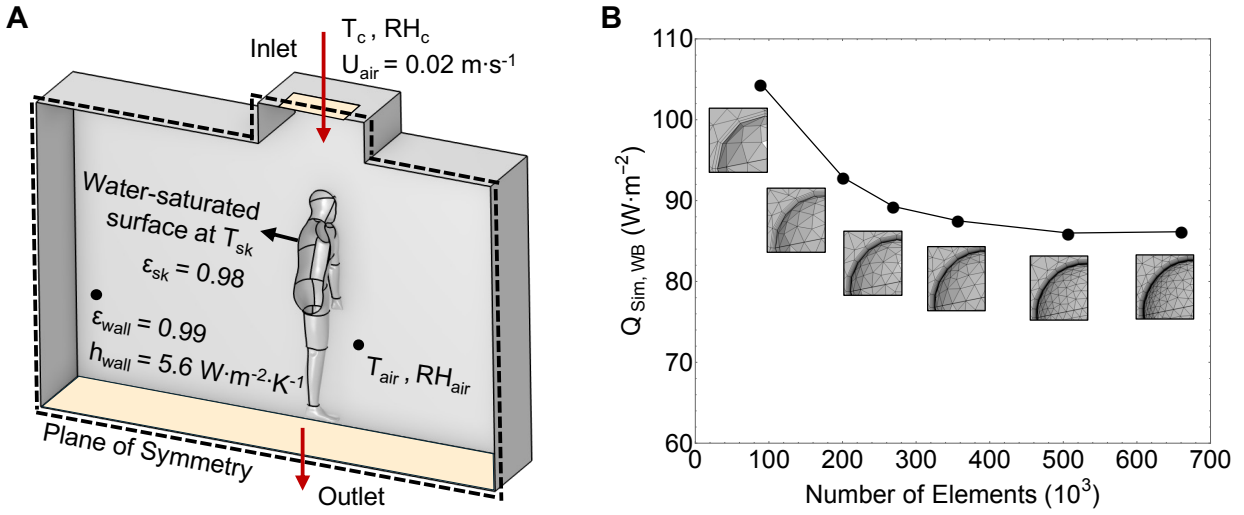


**Fig. S4. (A) Schematic and (B) Mesh refinement study of the coupled multiphysics model used for validation.**  $T_{sk}$  ( $^{\circ}\text{C}$ ) and  $\epsilon_{sk}$  – manikin's surface temperature and emissivity respectively,  $h_{wall}$  ( $\text{W}\cdot\text{m}^{-2}\cdot\text{K}^{-1}$ ) – equivalent heat transfer coefficient of the enclosure walls accounting for wall resistance and external convection,  $\epsilon_{wall}$  – wall emissivity,  $T_{air}$  ( $^{\circ}\text{C}$ ) and  $RH_{air}$  (%) – enclosure air temperature and relative humidity respectively,  $T_c$  ( $^{\circ}\text{C}$ ) and  $RH_c$  (%) – climatic chamber air temperature and relative humidity respectively,  $U_{air}$  ( $\text{m}\cdot\text{s}^{-1}$ ) – inlet air speed,  $Q_{Sim, WB}$  ( $\text{W}\cdot\text{m}^{-2}$ ) – whole-body total heat flux computed from the simulations.

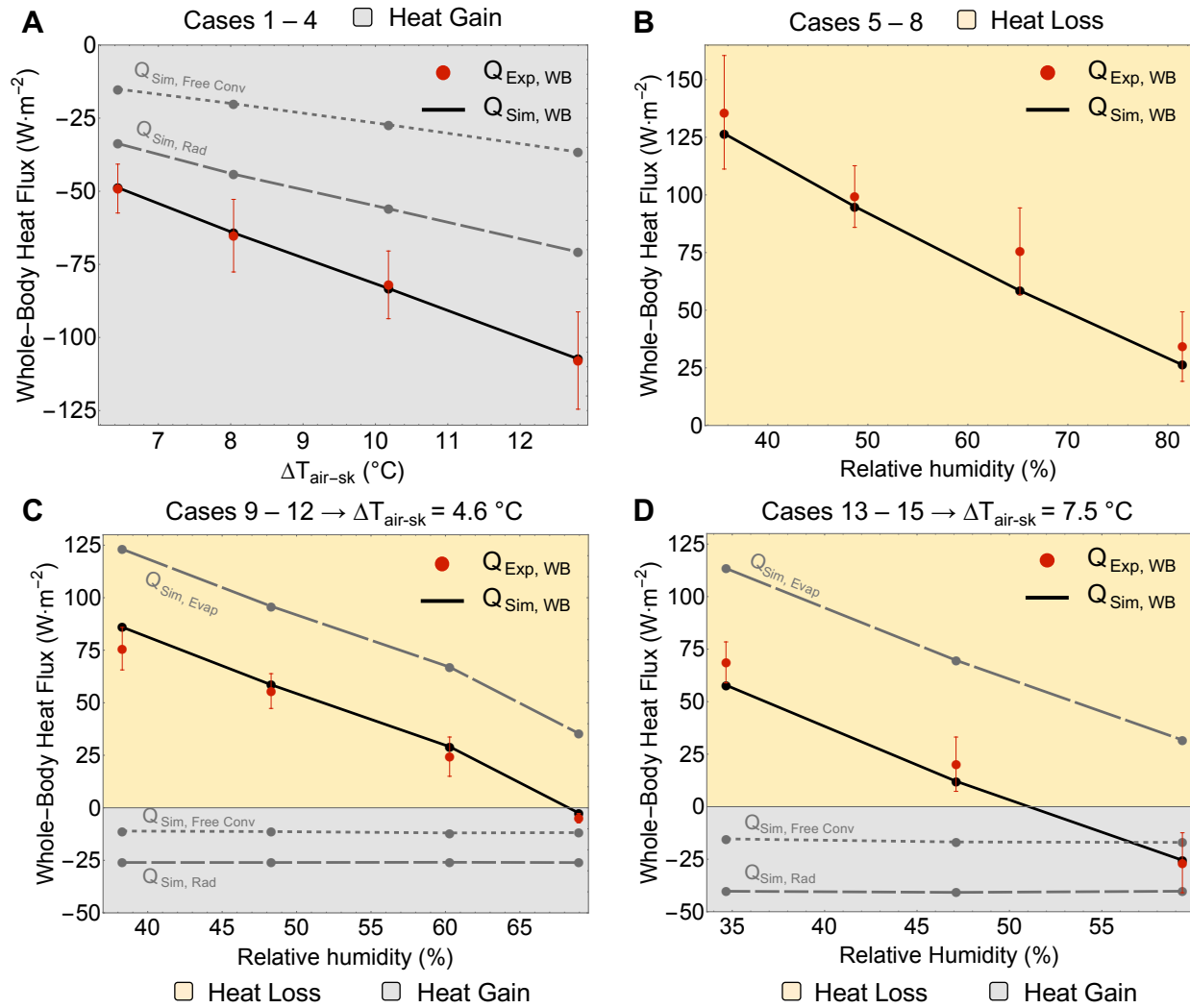


**Fig. S5. Comparison of whole-body heat fluxes between experiments and simulations.**  $Q_{\text{Exp, WB}}$  ( $\text{W}\cdot\text{m}^{-2}$ ) and  $Q_{\text{Sim, WB}}$  ( $\text{W}\cdot\text{m}^{-2}$ ) – whole-body total heat fluxes from experiments and simulations respectively. **(A)** Temperature-only driven free convection (Cases 1–4), **(B)** Humidity-only driven sweat evaporation (Cases 5–8), **(C–D)** Combined temperature and humidity-driven heat transfer (Cases 9–15). Strong agreement between experimental and simulated results at the whole-body level confirms the reliability of the coupled multiphysics model. Data points are averages of three replicates with 95% confidence intervals (combined Type A and B uncertainty).

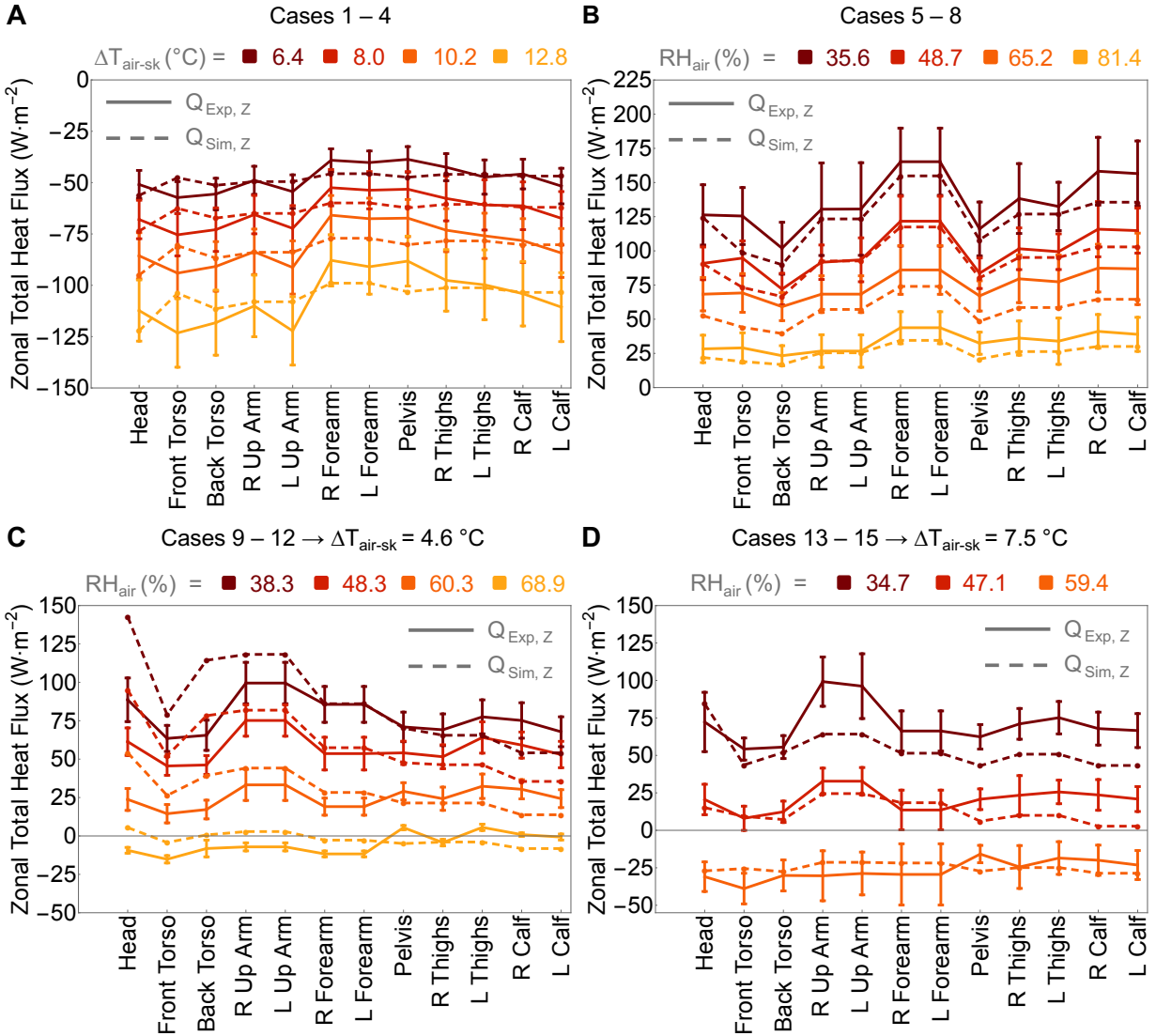


**Fig. S6. Comparison of zonal total heat fluxes between experiments and simulations.**  $Q_{Exp,Z}$  ( $W \cdot m^{-2}$ ) – Zonal measured total heat flux,  $Q_{Sim,Z}$  ( $W \cdot m^{-2}$ ) – Zonal simulated total heat flux **(A)** Temperature-only driven free convection (Cases 1–4), **(B)** Humidity-only driven sweat evaporation (Cases 5–8), **(C–D)** Combined temperature and humidity-driven heat transfer (Cases 9–15). Overall strong agreement, with minor discrepancies at specific zones, confirms the reliability of the coupled multiphysics model. Data points are averages of three replicates with 95% confidence intervals (combined Type A and B uncertainty).



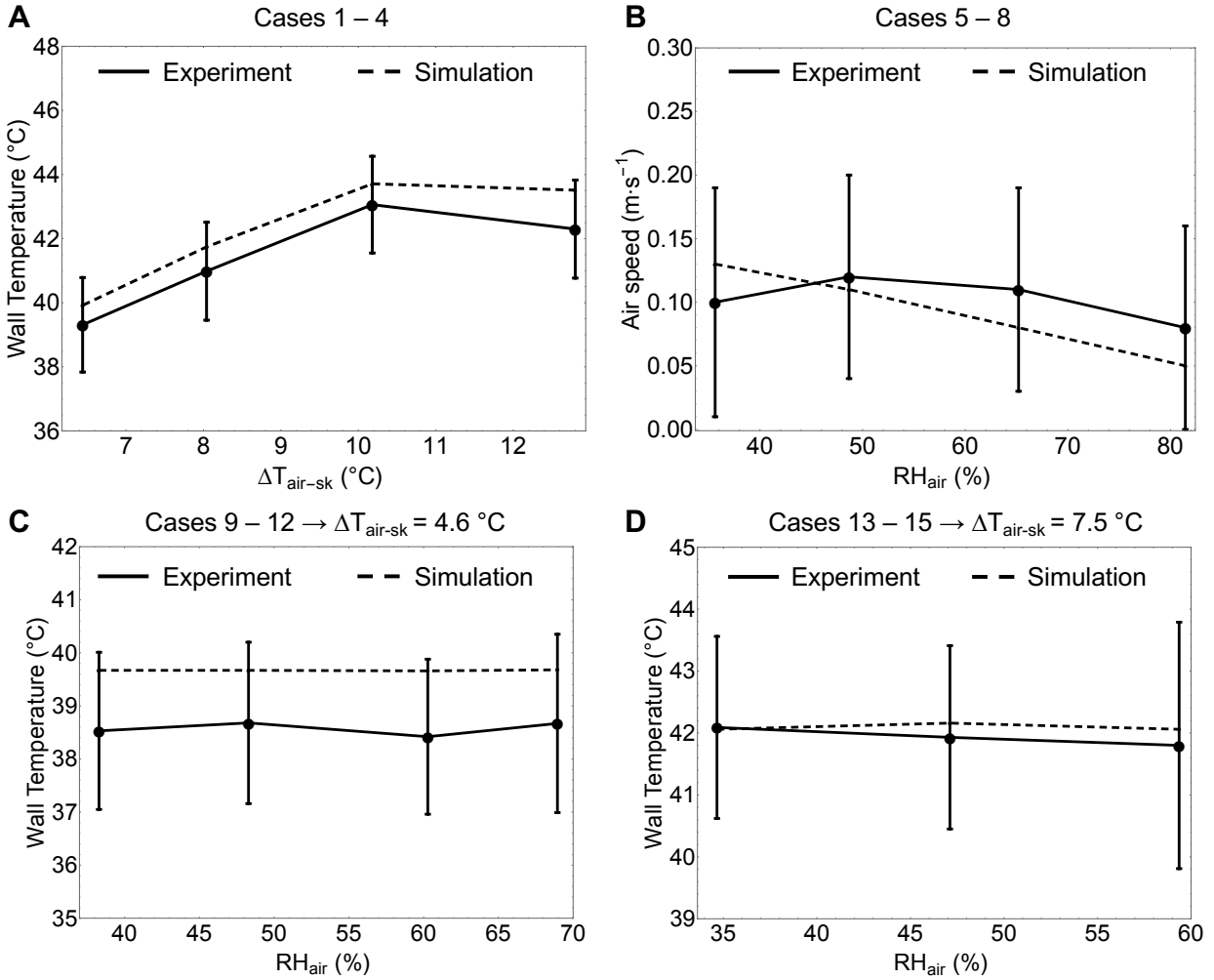


**Fig. S7. Comparison of key environmental parameters between experiments and simulations.** (A, C, D) Enclosure wall temperature (Fig. S3A) for temperature-only driven free convection (Cases 1–4), and combined temperature and humidity-driven heat transfer (Cases 9–15). (B) Air speed above the manikin’s head (Fig. S3E) for humidity-only driven sweat evaporation (Cases 5–8). All comparisons show good agreement, further confirming the reliability of the coupled multiphysics model. Data points are averages of three replicates with  $\pm 1$  SD (standard deviation) (combined Type A and B uncertainty).

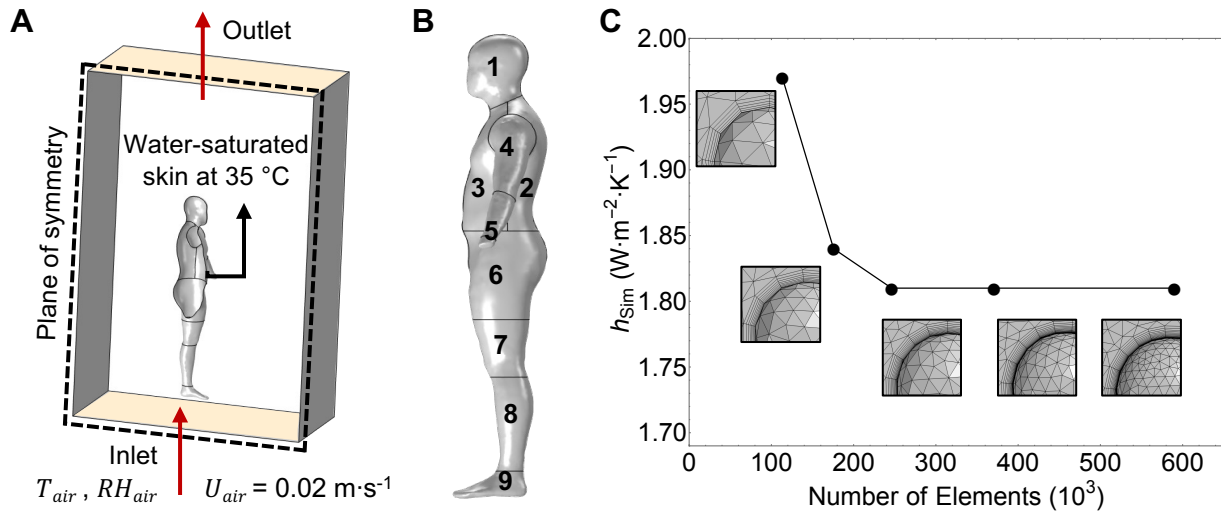


**Fig. S8. Development of multiphysics model for parametric study. (A)** Schematic of the digital twin,  $T_{air}$  ( $^{\circ}\text{C}$ ) and  $RH_{air}$  (%) – air temperature and relative humidity respectively,  $U_{air}$  ( $\text{m}\cdot\text{s}^{-1}$ ) – inlet air speed. **(B)** Cross-sectional side view of an average western young male (50<sup>th</sup> percentile height (m) and BMI ( $\text{kg}\cdot\text{m}^{-2}$ )) with 9 body segments. **(C)** Mesh refinement study of the validated coupled multiphysics model used for parametric study.  $h_{sim}$  ( $\text{W}\cdot\text{m}^{-2}\cdot\text{K}^{-1}$ ), – simulated whole-body free convective coefficient. Inset: Zoomed in pictures of how the boundary layer on the manikin's head grows denser with finer mesh sizes.

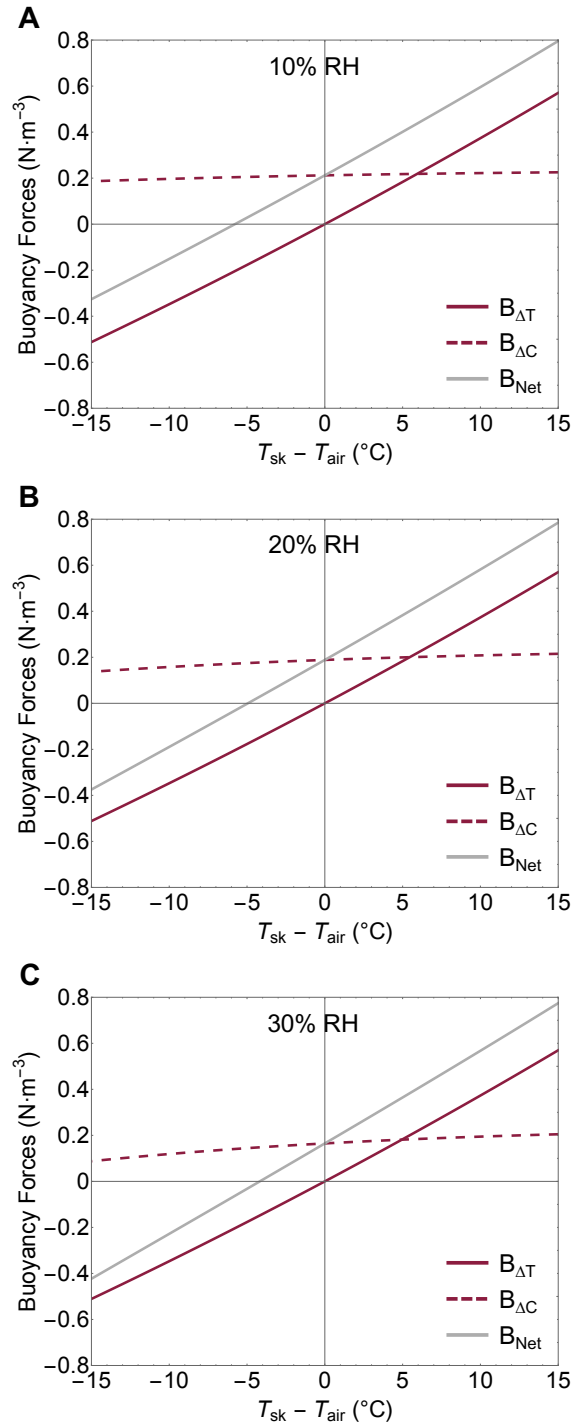


**Fig. S9. Comparison of different buoyancy forces across varying ambient conditions.** Individual buoyancy forces generated by temperature difference-driven ( $B_{\Delta T}$ , N·m<sup>-3</sup>), humidity or moisture concentration differences-driven ( $B_{\Delta C}$ , N·m<sup>-3</sup>) and their sum ( $B_{Net}$ , N·m<sup>-3</sup>) are compared across the entire air temperature range at **(A)** 10% RH, **(B)** 20% RH, and **(C)** 30% RH.  $T_{sk}$ — skin temperature (at 35 °C),  $T_{air}$ — air temperature (20–50 °C).

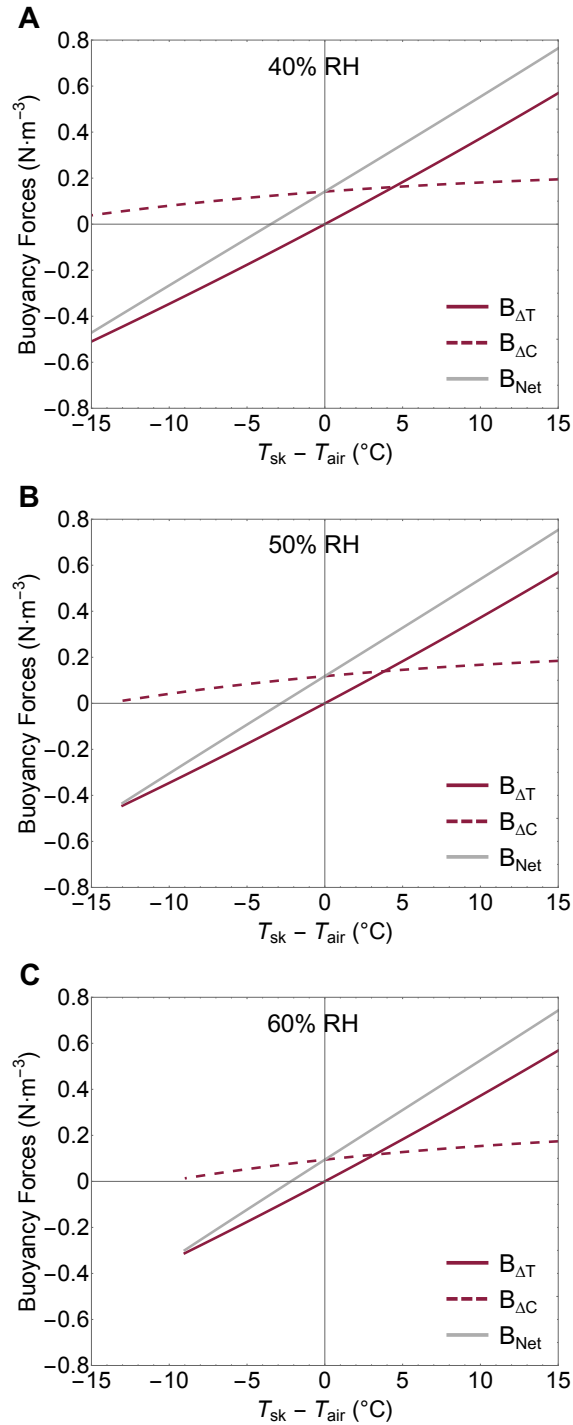


**Fig. S10. Comparison of different buoyancy forces across varying ambient conditions.** Individual buoyancy forces generated by temperature difference-driven ( $B_{\Delta T}$ , N·m<sup>-3</sup>), humidity or moisture concentration differences-driven ( $B_{\Delta C}$ , N·m<sup>-3</sup>) and their sum ( $B_{Net}$ , N·m<sup>-3</sup>) are compared across the entire air temperature range at (A) 40% RH, (B) 50% RH, and (C) 60% RH.  $T_{sk}$ —skin temperature (at 35 °C),  $T_{air}$ —air temperature (°C). Only cases with a positive skin-to-air moisture concentration difference ( $C_{sk} > C_{air}$ ) was computed; scenarios with  $C_{sk} < C_{air}$ —which would cause condensation on the skin—were omitted.

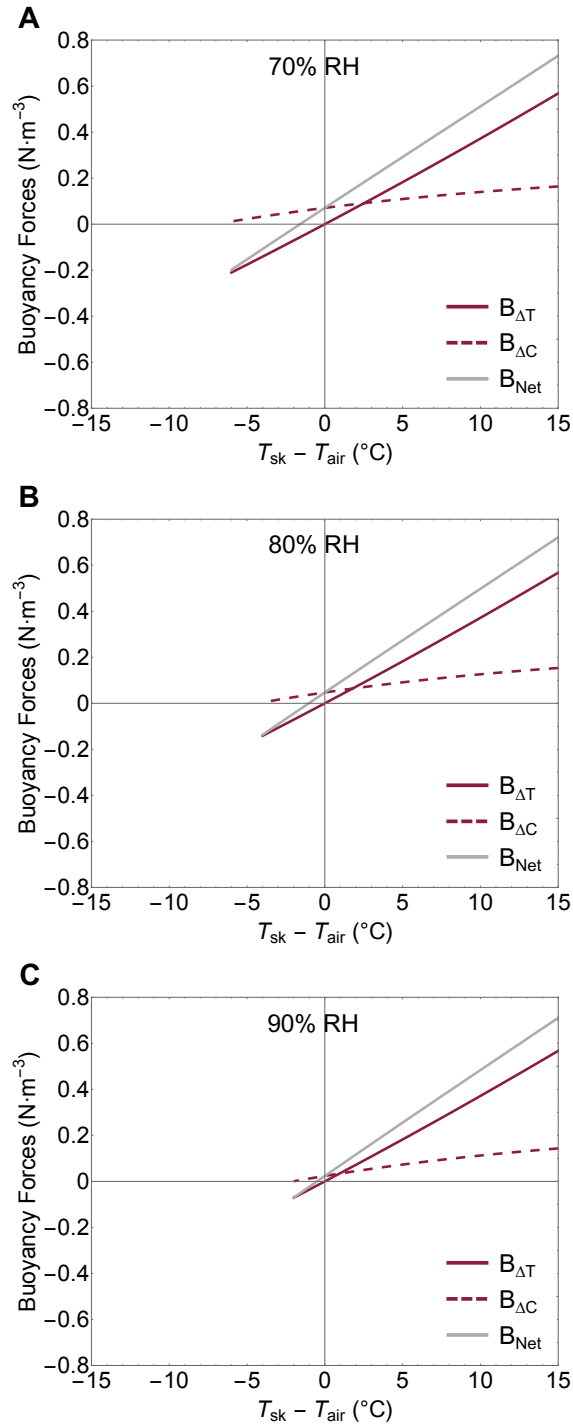


**Fig. S11. Comparison of different buoyancy forces across varying ambient conditions.** Individual buoyancy forces generated by temperature difference-driven ( $B_{\Delta T}$ , N·m<sup>-3</sup>), humidity or moisture concentration differences-driven ( $B_{\Delta C}$ , N·m<sup>-3</sup>) and their sum ( $B_{Net}$ , N·m<sup>-3</sup>) are compared across the entire air temperature range at **(A)** 40% RH, **(B)** 50% RH, and **(C)** 60% RH.  $T_{sk}$ — skin temperature (at 35 °C),  $T_{air}$ — air temperature (°C). Only cases with a positive skin-to-air moisture concentration difference ( $C_{sk} > C_{air}$ ) was computed; scenarios with  $C_{sk} < C_{air}$ —which would cause condensation on the skin—were omitted.

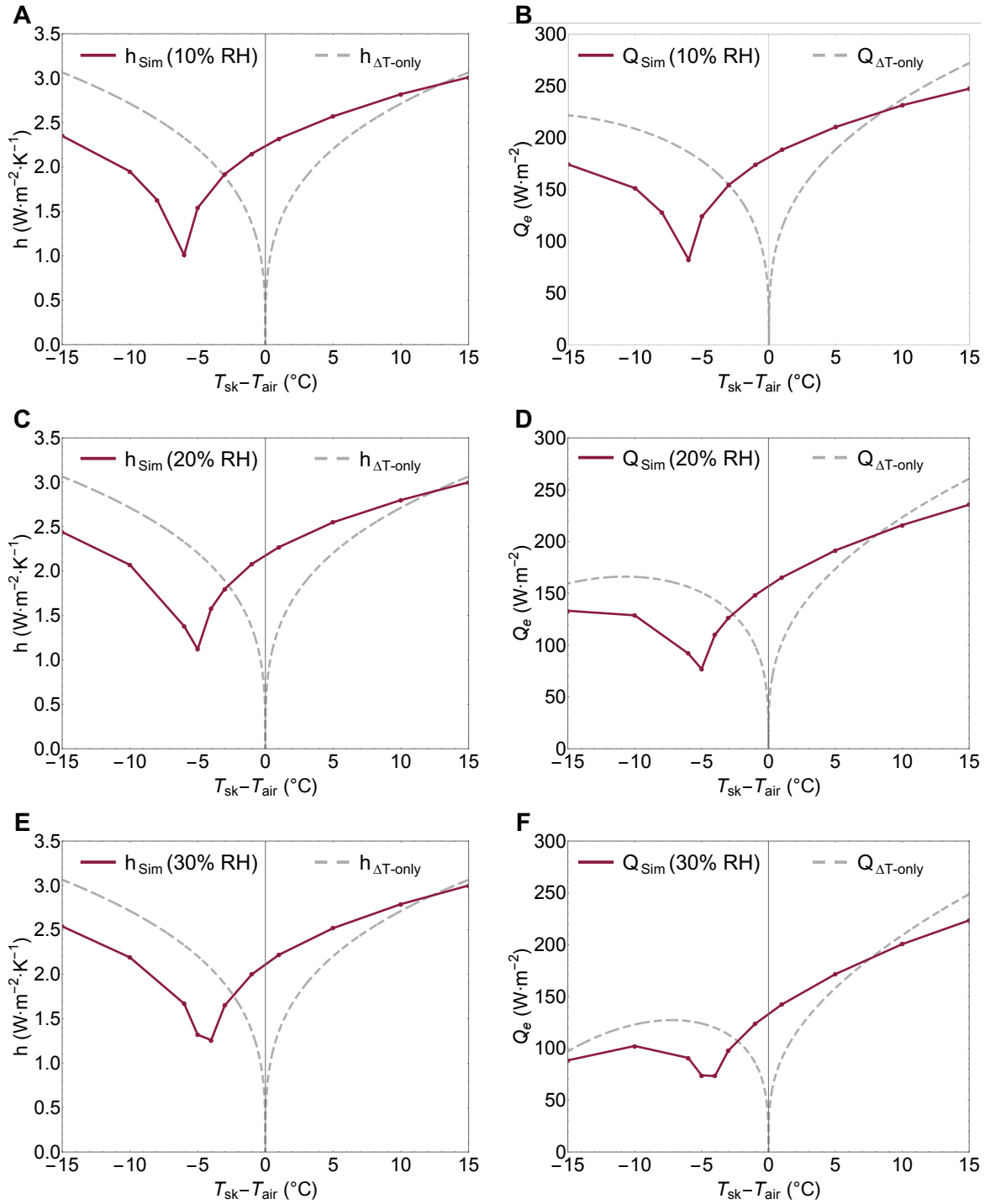


**Fig. S12. Comparison of simulated whole-body free convective coefficients and evaporative fluxes accounting for temperature- and humidity-differences against only temperature-difference only empirical correlations.**  $h_{Sim}$  (W·m<sup>-2</sup>·K<sup>-1</sup>) and  $Q_{Sim}$  (W·m<sup>-2</sup>) – Simulated whole-body free convective coefficients and evaporative fluxes respectively,  $h_{\Delta T-only}$  (W·m<sup>-2</sup>·K<sup>-1</sup>) and  $Q_{\Delta T-only}$  (W·m<sup>-2</sup>) – thermal-gradient only empirical correlations (Eq. S8–S9) respectively, (A–B) 10%  $RH_{air}$ , (C–D) 20%  $RH_{air}$ , (E–F) 30%  $RH_{air}$

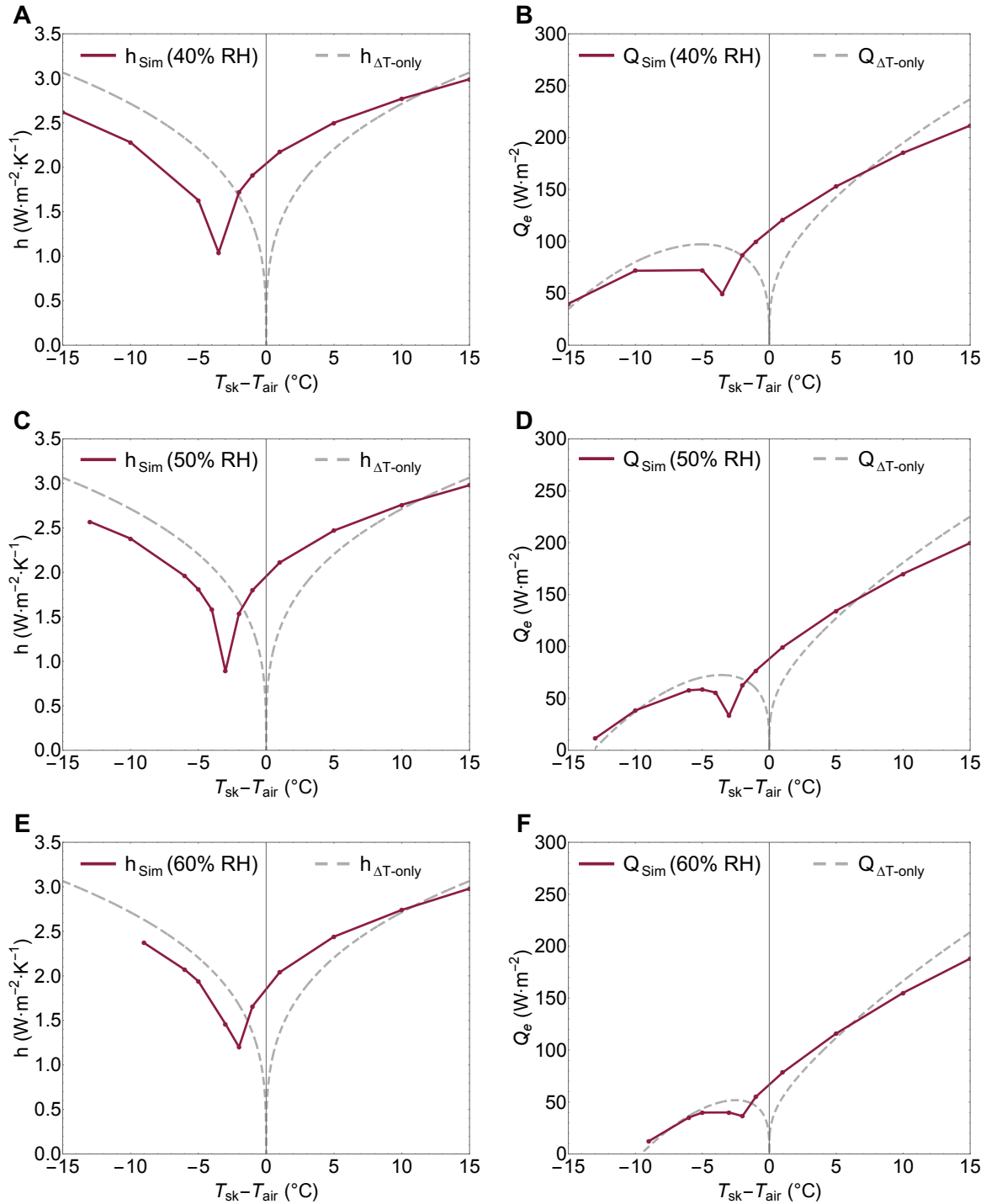


**Fig. S13. Comparison of simulated whole-body free convective coefficients and evaporative fluxes accounting for temperature- and humidity-differences against only temperature-difference only empirical correlations.**  $h_{Sim}$  (W·m<sup>-2</sup>·K<sup>-1</sup>) and  $Q_{Sim}$  (W·m<sup>-2</sup>) – Simulated whole-body free convective coefficients and evaporative fluxes respectively,  $h_{\Delta T-only}$  (W·m<sup>-2</sup>·K<sup>-1</sup>) and  $Q_{\Delta T-only}$  (W·m<sup>-2</sup>) – thermal-gradient only empirical correlations (Eq. S8–S9) respectively, (A–B) 40%  $RH_{air}$ , (C–D) 50%  $RH_{air}$ , (E–F) 60%  $RH_{air}$

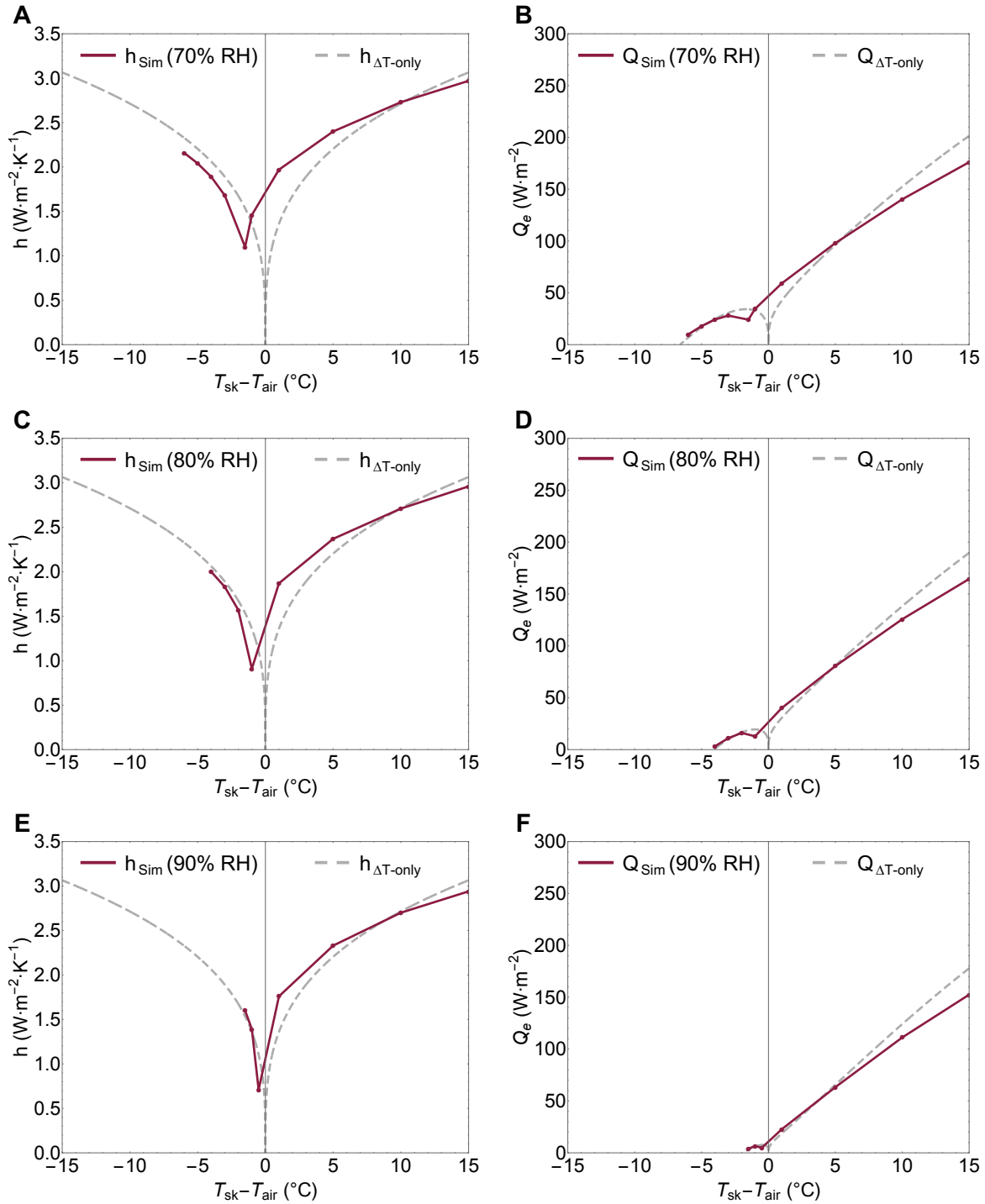


**Fig. S14. Comparison of simulated whole-body free convective coefficients and evaporative fluxes accounting for temperature- and humidity-differences against only temperature-difference only empirical correlations.**  $h_{Sim}$  (W·m<sup>-2</sup>·K<sup>-1</sup>) and  $Q_{Sim}$  (W·m<sup>-2</sup>) – Simulated whole-body free convective coefficients and evaporative fluxes respectively,  $h_{\Delta T-only}$  (W·m<sup>-2</sup>·K<sup>-1</sup>) and  $Q_{\Delta T-only}$  (W·m<sup>-2</sup>) – thermal-gradient only empirical correlations (Eq. S8–S9) respectively, (A–B) 70%  $RH_{air}$ , (C–D) 80%  $RH_{air}$ , (E–F) 90%  $RH_{air}$



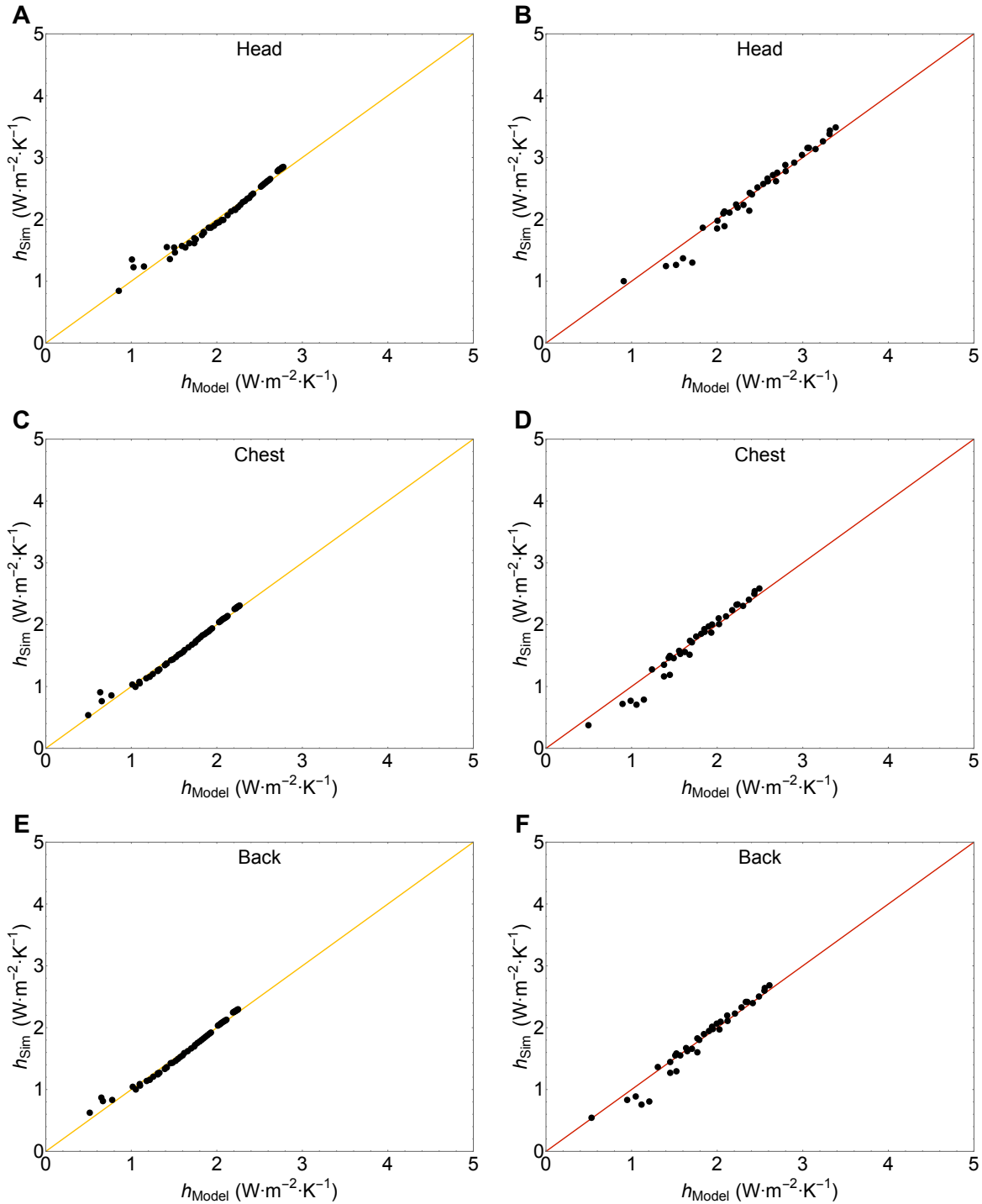


**Fig. S15. Zonal comparison of simulated free convective coefficients against the physics-informed model.** Simulated free convective coefficients ( $h_{Sim}$ ,  $W \cdot m^{-2} \cdot K^{-1}$ ) are compared with the model predictions ( $h_{Model}$ ,  $W \cdot m^{-2}$ ) from Eq. S10 across (A–B) Head, (C–D) Chest, (E–F) Back. For each zone, left panels correspond to positive (supporting) combined temperature and concentration buoyancy ( $\Delta T_{sk-air} + 164C_{sk-air}$ ), and right panels correspond to negative (opposing) buoyancy. The strong agreement demonstrates that the physics-informed model robustly captures zonal free convection across both buoyancy regimes.

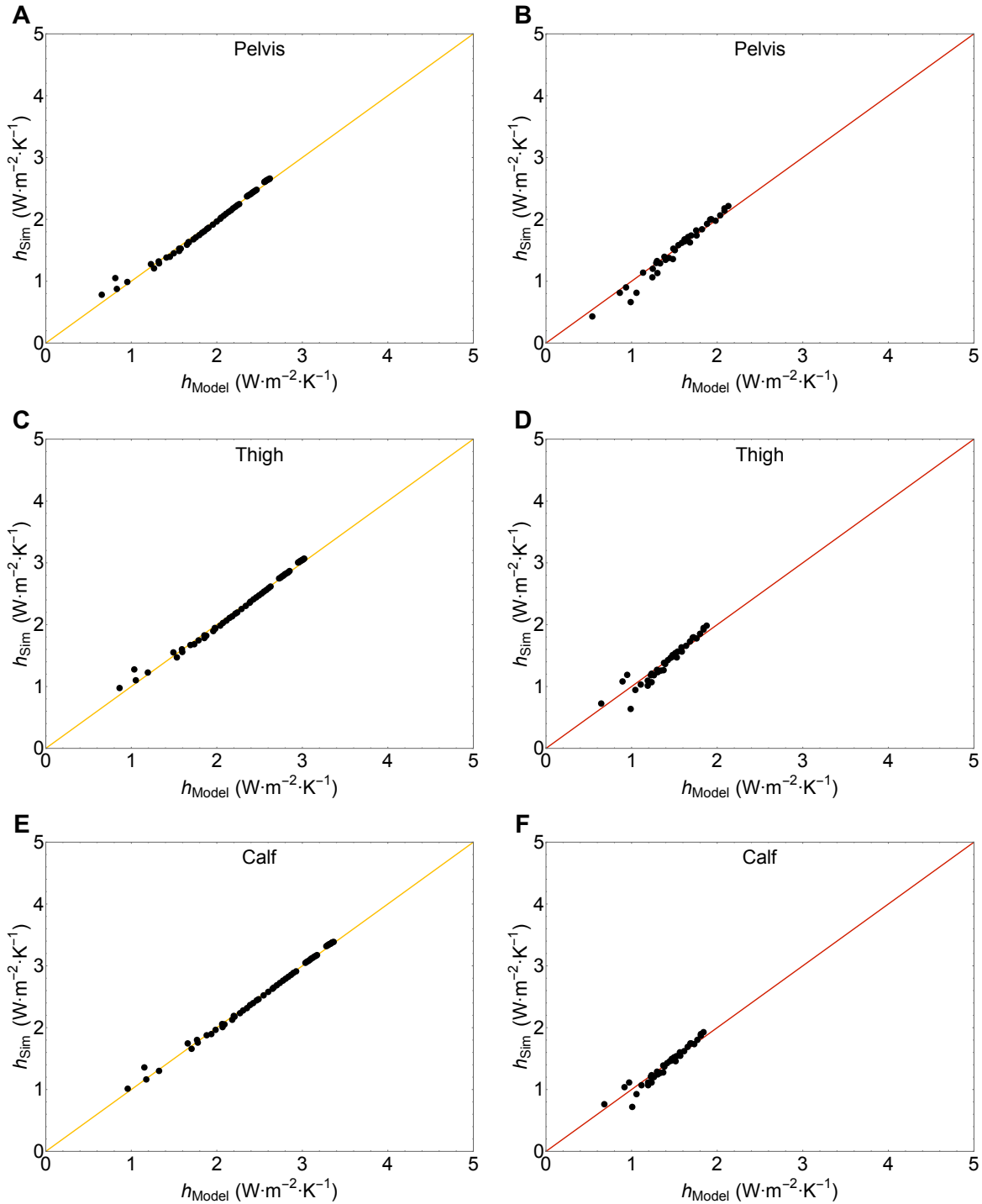


**Fig. S16. Zonal comparison of simulated free convective coefficients against the physics-informed model.** Simulated free convective coefficients ( $h_{Sim}$ ,  $W \cdot m^{-2} \cdot K^{-1}$ ) are compared with the model predictions ( $h_{Model}$ ,  $W \cdot m^{-2}$ ) from Eq. S10 across (A–B) Pelvis, (C–D) Thigh, (E–F) Calf. For each zone, left panels correspond to positive (supporting) combined temperature and concentration buoyancy ( $\Delta T_{sk-air} + 164C_{sk-air}$ ), and right panels correspond to negative (opposing) buoyancy. The strong agreement demonstrates that the physics-informed model robustly captures zonal free convection across both buoyancy regimes.

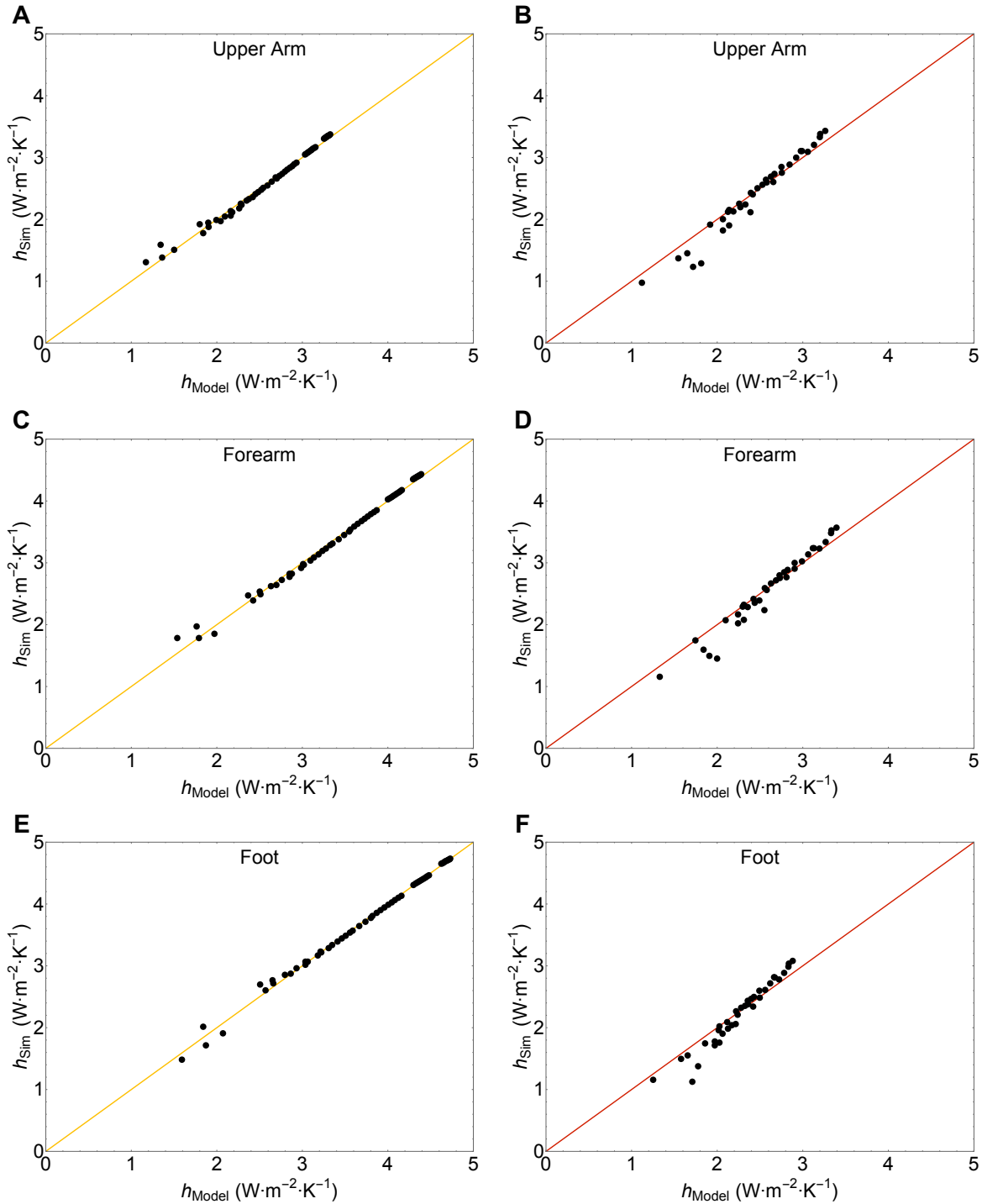


**Fig. S17. Zonal comparison of simulated free convective coefficients against the physics-informed model.** Simulated free convective coefficients ( $h_{Sim}$ ,  $W \cdot m^{-2} \cdot K^{-1}$ ) are compared with the model predictions ( $h_{Model}$ ,  $W \cdot m^{-2}$ ) from Eq. S10 across (A–B) Upper arm, (C–D) Forearm, (E–F) Foot. For each zone, left panels correspond to positive (supporting) combined temperature and concentration buoyancy ( $\Delta T_{sk-air} + 164C_{sk-air}$ ), and right panels correspond to negative (opposing) buoyancy. The strong agreement demonstrates that the physics-informed model robustly captures zonal free convection across both buoyancy regimes.

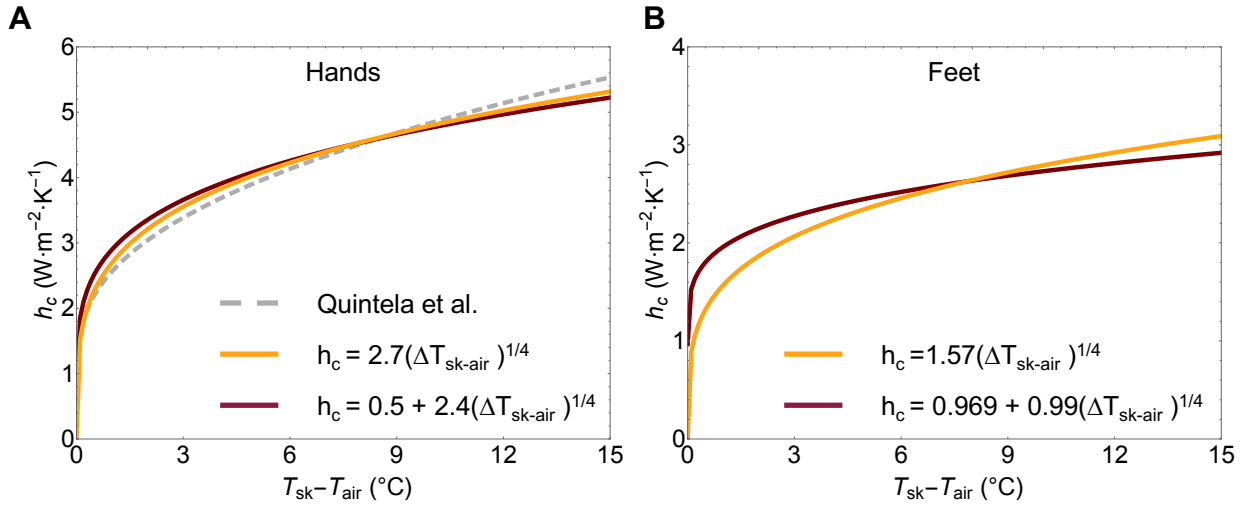


**Fig. S18. Comparison of fitted free convective correlations for hands and feet. (A) Hand:** Simulated free convective coefficients ( $h_c$ ,  $\text{W}\cdot\text{m}^{-2}\cdot\text{K}^{-1}$ ) for hands were fitted using temperature-difference scaling (Eq. S11) and combined temperature- and concentration-difference scaling (Eq. S12) and compared with average correlations from Quintela et al. (13) (Eq. S13–S14). **(B) Feet:**  $h_c$  for feet fitted with temperature-difference scaling (Eq. S15) compared with combined temperature- and concentration- difference scaling (Eq. S16)

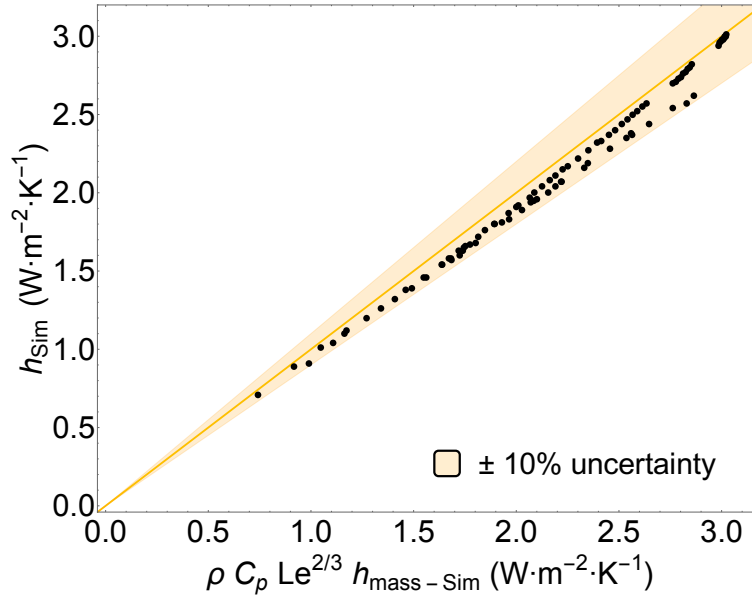


**Fig. S19. Comparison of simulated whole-body free convective coefficients and mass transfer-derived equivalents and validating the Chilton-Colburn analogy.** Simulated whole-body mass transfer coefficients ( $h_{mass-Sim}$ ,  $\text{m}\cdot\text{s}^{-1}$ ) were multiplied by moist air density ( $\rho$ ,  $\text{kg}\cdot\text{m}^{-3}$ ), specific heat ( $C_p$ ,  $\text{J}\cdot\text{kg}^{-1}\cdot\text{K}^{-1}$ ), and Lewis number ( $Le$ , dimensionless) (Eq. S1) to estimate the mass transfer-derived equivalents of  $h_{Sim}$  ( $\text{W}\cdot\text{m}^{-2}\cdot\text{K}^{-1}$ ). A strong agreement shows that Chilton-Colburn analogy holds under free convective conditions only when  $h_{Sim}$  accounts for coupled temperature and humidity-differences.

**Table S1. Detailed specifications of the instruments used to measure the inlet air temperature ( $T_{air}$ ), relative humidity ( $RH_{air}$ ), and air speed ( $v_{air}$ ) within the enclosure.**

<b>Sensor</b>	<b>Manufacturer</b>	<b>Variable (s) Measured</b>	<b>Quantity</b>	<b>Uncertainty</b>	<b>Frequency (Hz)</b>
EE181	Campbell Scientific, Inc.	$T_{air}$ & $RH_{air}$	1	$\pm 0.2$ °C $\pm (1.4 + 0.01 \text{ RH}) \%$	1
Senso Anemo5100 LSF Transducer	Sensor Electronic	$v_{air}$	5	$\pm 0.02$ m·s <sup>-1</sup>	8

**Table S2. Detailed specifications of the sensors used to measure air temperature ( $T_{air}$ ), wall temperatures ( $T_{wall}$ ), relative humidity ( $RH_{air}$ ), and air velocity ( $v_{air}$ ) inside the enclosure. The manufacturer specified the uncertainties of the 3D sonic anemometer in absolute terms and the 2D sonic wind sensor in relative terms.**

<b>Sensor</b>	<b>Manufacturer</b>	<b>Variable (s) Measured</b>	<b>Quantity</b>	<b>Uncertainty</b>	<b>Frequency (Hz)</b>
CSAT3B	Campbell Scientific, Inc.	$v_{air}$	1	$\pm 0.08 \text{ m}\cdot\text{s}^{-1}$ ( $U_x, U_y$ ) $\pm 0.04 \text{ m}\cdot\text{s}^{-1}$ ( $U_z$ )	1
WINDSONIC1-L	Campbell Scientific, Inc.	$v_{air}$	1	$\pm 2\%$	1
EE181	Campbell Scientific, Inc.	$T_{air}$ & $RH_{air}$	1	$\pm 0.2 \text{ }^\circ\text{C}$ $\pm (1.4 + 0.01 \text{ RH}) \%$	0.33
Type-T Thermocouple	Minnesota Measurement Instruments LLC	$T_{wall}$	2	$\pm 0.5 \text{ }^\circ\text{C}$	1

**Table S3. Summary of enclosure's environmental and manikin skin conditions for each experimental case.  $T_c$  &  $RH_c$  – air temperature and relative humidity setpoints of the climatic chamber,  $T_{air}$  &  $RH_{air}$  – air temperature and relative humidity measured within the enclosure (Fig. S1.B–C),  $T_{sk}$  – manikin skin temperature,  $\Delta T_{air-sk}$  – temperature difference between  $T_{air}$  &  $T_{sk}$**

Cases	$T_c$ (°C)	$RH_c$ (%)	$T_{air}$ (°C)	$RH_{air}$ (%)	$T_{sk}$ (°C)	Skin wettedness	$\Delta T_{air-sk}$ (°C)
<b>Temperature-only driven free convection (Dry free convection and radiation only)</b>							
1	40	24.6	40.4 ± 0.2	27.6 ± 1.9	34	0	6.4 ± 0.2
2	42	22.2	42.0 ± 0.2	25.4 ± 2.3	34	0	8.0 ± 0.2
3	44	20	44.2 ± 0.2	23.5 ± 1.6	34	0	10.2 ± 0.2
4	44	20	43.8 ± 0.2	23.8 ± 1.6	31	0	12.8 ± 0.2
<b>Humidity-only driven sweat evaporation only</b>							
5	35	27	35.3 ± 0.2	35.6 ± 1.5	35.0 ± 0.2	1	0.3 ± 0.1
6	35	44	35.3 ± 0.2	48.7 ± 1.5	35.0 ± 0.1	1	0.3 ± 0.1
7	35	60	35.5 ± 0.2	65.2 ± 1.5	35.4 ± 0.1	1	0.1 ± 0.1
8	35	80	35.5 ± 0.2	81.4 ± 1.5	35.4 ± 0.1	1	0.1 ± 0.1
<b>Combined temperature and humidity effects (Free convection, radiation and sweat evaporation)</b>							
9	40	19	39.6 ± 0.2	38.3 ± 1.6	35.0	1	4.6 ± 0.2
10	40	34	39.6 ± 0.2	48.3 ± 1.5	35.0	1	4.6 ± 0.2
11	40	45	39.5 ± 0.2	60.3 ± 1.9	35.0	1	4.5 ± 0.2
12	40	61	39.6 ± 0.2	68.9 ± 1.6	35.0	1	4.6 ± 0.2
13	44	22	42.4 ± 0.2	34.7 ± 1.7	35.0	1	7.4 ± 0.2
14	44	34	42.5 ± 0.2	47.1 ± 2.0	35.0	1	7.5 ± 0.2
15	44	49	42.4 ± 0.2	59.4 ± 2.0	35.0	1	7.4 ± 0.2



**Table S4. Summary of the behavior of temperature- and humidity-induced buoyancies across air temperature regimes.  $T_{sk}$  (°C) and  $T_{air}$  (°C) are the skin and air temperatures respectively,  $C_{sk}$  (kg·m<sup>-3</sup>) and  $C_{air}$  (kg·m<sup>-3</sup>) are the corresponding water-vapor concentrations,  $\Delta T_{sk-air}$  (°C) and  $\Delta C_{sk-air}$  (kg·m<sup>-3</sup>) are the skin-to-air temperature and concentration differences, respectively.  $B_{\Delta T} = g\rho\beta_T\Delta T_{sk-air}$  and  $B_{\Delta C} = g\rho\beta_C\Delta C_{sk-air}$ , are the thermal- and concentration-driven buoyancies respectively, where  $g$  is the gravitational acceleration (9.81 m·s<sup>-2</sup>),  $\beta_T$  is the thermal coefficient of expansion (reciprocal of the absolute average of  $T_{air}$  and  $T_{sk}$ ), and  $\beta_C$  is the coefficient of expansion due to compositional changes. Net buoyancy  $B_{net}$  is the sum of  $B_{\Delta C}$  and  $B_{\Delta T}$ . Stagnation temperature  $T_{stag}$  is the air temperature at which  $B_{\Delta C}$  and  $B_{\Delta T}$  cancel out, producing a near stagnant flow for a particular  $RH_{air}$**

<b>Regime</b>	$\Delta T_{sk-air}$	$\Delta C_{sk-air}$	$B_{\Delta T}$	$B_{\Delta C}$	<b>Dominant force</b>	$B_{net}$	<b>Plume Direction</b>
$T_{air} < T_{sk}$	> 0	> 0	> 0	> 0	$B_{\Delta T}$	$B_{\Delta C} + B_{\Delta T}$	Up
$T_{sk} < T_{air} < T_{stag}$	< 0	> 0	< 0	> 0	$B_{\Delta C}$	$B_{\Delta C} - B_{\Delta T}$	Up
$T_{sk} < T_{air} = T_{stag}$	< 0	> 0	< 0	> 0	$B_{\Delta T} \approx B_{\Delta C}$	~0	Nearly stagnant
$T_{air} > T_{stag} > T_{sk}$	< 0	> 0	< 0	> 0	$B_{\Delta T}$	$B_{\Delta C} - B_{\Delta T}$	Down

## SI References

1. Y. A. 'Ghajar, A. J. ' Çengel, *Heat and Mass Transfer: Fundamentals and Applications, 5th ed. New York, NY.* (McGraw-Hill, 2014), pp. 874–880.
2. E. H. Wissler, *Human Temperature Control* (Springer Berlin Heidelberg, 2018), pp. 346–349.
3. Ken Parsons, *Human thermal environments: the effects of hot, moderate, and cold environments on human health, comfort and performance* (CRC Press, 2014), pp. 166–167.
4. S. H. Viswanathan, *et al.*, Impact of human body shape on free convection heat transfer. *PLoS One* 20, e0318842 (2025).
5. A. Joshi, *et al.*, Evaluation of thermal properties and thermoregulatory impacts of lower back exosuit using thermal manikin. *Int J Ind Ergon* 98 (2023).
6. K. Rykaczewski, *et al.*, A simple three-cylinder radiometer and low-speed anemometer to characterize human extreme heat exposure. *Int J Biometeorol* 68, 1081–1092 (2024).
7. A. Joshi, *et al.*, Characterization of human extreme heat exposure using an outdoor thermal manikin. *Science of the Total Environment* 923 (2024).
8. K. Sadeghi, *et al.*, Resolving shortwave and longwave irradiation distributions across the human body in outdoor built environments. *Build Environ* 277 (2025).
9. M. Fojtlín, J. Fišer, M. Jícha, Determination of convective and radiative heat transfer coefficients using 34-zones thermal manikin: Uncertainty and reproducibility evaluation. *Exp Therm Fluid Sci* 77, 257–264 (2016).
10. COMSOL Multiphysics. CFD Module User's Guide. Available at <https://doc.comsol.com/6.2/doc/com.comsol.help.cfd/CFDModuleUsersGuide.pdf>, pp. 256–257 (accessed 19 November 2025).
11. B. Gebhart, L. Pera, The nature of vertical natural convection flows resulting from the combined buoyancy effects of thermal and mass diffusion. *Int J Heat Mass Transf* 14, 2025–2050 (1971).
12. D. M. Jennewein, *et al.*, The Sol Supercomputer at Arizona State University in *Practice and Experience in Advanced Research Computing*, (ACM, 2023), pp. 296–301.
13. D. Quintela, A. Gaspar, C. Borges, Analysis of sensible heat exchanges from a thermal manikin. *Eur J Appl Physiol* 92, 663–668 (2004).